JEM–X Scientific Analysis:
Scientific Validation Report

Version 5.0

Niels Jørgen Westergaard, Carol Anne Oxborrow
Jérôme Chenevez, Niels Lund, Søren Brandt,
Carl Budtz-Jørgensen, Peter Kretschmar, Stefan Larsson,
and Silvia Martínez-Núñez

June 8, 2005

DANISH NATIONAL
SPACE CENTER

Contents

Table of contents i
List of changes iii
List of figures iv

1 Introduction **1**
1.1 Scope of the Document 1
1.2 Applicable Documents 3
1.3 Acronyms and Abbreviations 6

2 Data correction **7**
2.1 Energy calibration 7
2.2 Evolution of gain 15
2.3 Evolution of energy resolution 15
2.4 Dead time and grey filter 19
2.5 Timing 21
2.5.1 Absolute timing 21
2.5.2 Relative timing 21
2.6 Event quality filtering 21

3 Background determination **23**

4 Non-imaging results **28**
4.1 Detector spectra 28
4.2 Detector light-curves 28

5 Imaging **31**

6 Source detection **34**

6.1 Source positions 34

6.2 Source detection significance 37

6.3 Source fluxes 39

7 Source property extraction **42**

7.1 Source Spectra 42

7.1.1 The Crab Nebula as calibration source 43

7.1.2 The spectrum of a weak source 45

7.2 Source Light Curves 45

7.3 Error estimates 50

8 Future Improvements **52**

Issue	Revision	Date	Comments
1	0	2002-08-23	First version
2	0	2003-07-01	For OSA2
3	0	2004-12-05	For OSA3
4	0	2004-07-15	For OSA4

List of Figures

2.1 Spatial gain variation of JEM–X1 given in percents from the average. 9
2.2 Spatial gain variation of JEM–X2 given in percents from the average. 10
2.3 Spatial gain variation of JEM–X1 for individual anodes, expressed as factor relative to the mean. 11
2.4 Spatial gain variation of JEM–X2 for individual anodes, expressed as factor relative to the mean. 12
2.5 Spectrum of JEM–X1 with spatial and anode corrections 13
2.6 Spectrum of JEM–X2 with spatial and anode corrections 13
2.7 Gain for JEM–X2 anodesection 3 in rev. 87–90 14
2.8 Peak position of energy calibration sources for JEM–X1 16
2.9 Peak position of energy calibration sources for JEM–X2 17
2.10 Energy resolution of JEM–X1 at Xe line 18
2.11 Energy resolution of JEM–X2 at Xe line 18
2.12 Typical dead time behaviour of JEM–X2 with grey filtering 20
2.13 Event status distribution 22

3.1 Background spectra of JEMX–X2 during revolution 41 25
3.2 JEMX–X1 detector background shadowgram 26
3.3 JEMX–X2 detector background shadowgram 27

4.1 JEM–X1 detector spectrum of a blank field observation 29
4.2 JEM–X2 detector spectrum of a blank field observation 29
4.3 Grey filter values and accepted data events 30
4.4 Detector lightcurve of Crab observation, revolution 39 30

5.1 Basic reconstruction image of Cen X–3 32
5.2 Fine resolution image of Cen X–3 33

6.1 Position deviations of Crab 35
6.2 Position deviations of Crab as function of angle 35
6.3 Position deviations as a function of det. significance 36
6.4 Found position deviations of Vela X-1 37
6.5 Significance of Crab detections with off-axis angle 38
6.6 Flux of Crab with off-axis angle 40
6.7 Derived flux of Crab versus instrument deadtime correction factor. 41

7.1 Crab spectral slope versus off-axis angle 43
7.2 Crab normalization versus off-axis angle 44
7.3 Remaining systematic deviations in Crab spectra 44
7.4 Spectrum of EXO2030+375 in the range 5 to 25 keV 45
7.5 Pulse profile of EXO2030+375 46
7.6 Light curve of Crab pulsar in revolution 39 47
7.7 Period folding analysis of Crab pulsar in revolution 39 48
7.8 Pulse profile of Crab pulsar in revolution 39 49
7.9 Error bars of a bright source 50
7.10 Error bars of a faint source, simple errors 51
7.11 Error bars of a faint source, equal errors 51

Chapter 1

Introduction

This is the JEM–X Analysis Scientific Validation Report (SVR). It describes the scientific results that can be expected from processing JEM–X data from the INTEGRAL satellite using the software installed at ISDC specifically for this purpose. This document should attempt to answer the question: how good are the results a user can expect from JEM–X and the ISDC system?

This document also describes some of the limitations that the technical details of the detector electronics and telemetry impose on the results.

N.B. It is strongly recommended that this document is viewed and printed in colour since it contains many figures where colour is essential to the data presented.

1.1 Scope of the Document

The results presented as examples of real scientific data in this document have been obtained by analysing data from various pointings of INTEGRAL using the Offline Scientific Analysis software (OSA) version 4.0 to be released by ISDC July 2004. This software can be downloaded from:
`http://isdc.unige.ch/index.cgi?Soft+download`
OSA is also known as IDAS_SW (INTEGRAL Data Analysis System Software). In some cases OSA3 results have been kept where the change to OSA4 is unimportant.

The analyses have been carried out by the members of the Scientific Data Analysis Team (SDAST) who wrote the software now installed at ISDC. SDAST consists of:

Jérôme Chenevez DSRI, Copenhagen, Denmark.
`jerome@dsri.dk`
Responsible for problem anode handling and monitoring, spectral analysis.

Peter Kretschmar MPE, Munich, Germany and ISDC, Geneva, Switzerland.
peter.kretschmar@obs.unige.ch
Responsible for data binning and pipeline scripts.

Stefan Larsson University Observatory, Stockholm, Sweden.
stefan@astro.su.se
Responsible for source extraction of spectra and lightcurves.

Sami Maisala University Observatory, Helsinki, Finland.
smaisala@astro.helsinki.fi
Responsible for background modelling.

Silvia Martínez-Núñez GACE, University of Valencia, Spain.
silvia.martinez@uv.es
Responsible for pipeline scripts.

Carol Anne Oxborrow DSRI, Copenhagen, Denmark.
oxborrow@dsri.dk
Responsible for automatic calibration and correction, and dead time analysis.

Niels Jørgen Westergaard DSRI, Copenhagen, Denmark.
njw@dsri.dk
Responsible for image deconvolution and source finding.

The JEM–X instrument team at DSRI has also taken part in these analyses and document writing:

Niels Lund nl@dsri.dk
PI for JEM–X. Responsible for IROS image deconvolution.

Søren Brandt sb@dsri.dk
Responsible for monitoring and analysis of instrument behavior.

Carl Budtz-Jørgensen carl@dsri.dk
Responsible for the detectors.

Additional help in the Scientific Validation has been supplied by:

Tim Oosterbroek RSSD, ESA Estec, Netherlands.
toosterb@rssd.esa.int

The main periods where data have been used for the analysis presented in this report are listed in the following table:

Description	Period	Revolutions
PV phase	2002-10-17 – 2002-12-30	1 – 20
Calibration period 3	2002-11-27 – 2003-02-25	14 – 44
Calibration period 4	2003-02-25 – 2003-05-22	45 – 73
Calibration period 5	2003-05-22 – 2004-02-16	74 – 164
Calibration period 6	2004-02-16 – ?	165 – ?

There has been a small number of instrument configuration updates such as changes in the event rejection criteria that have led to changes in the responses, in particular at low energy. The calibration periods span between such updates, except the dividing between period 4 and 5 which is artificial. A calibration using the Crab Nebula defines the response in each period except in the very beginning of the INTEGRAL mission where no good calibration can be done.

Currently there are known limitations in the software, and these will be discussed in the document where appropriate. The next full release of OSA is planned for December 2004.

The result of data analysis in the ISDC system depends on the choice of various processing parameters chosen by the user. In this document we try to give some guidelines about the use of various input parameters, their advantages and drawbacks.

1.2 Applicable Documents

The documents in bibliography on the next page have each an indication (in parenthesis) of where they can be found. A full explanation is given immediately below the bibliography.

Anyone wishing to do their own INTEGRAL data analysis should get hold of the Introduction to the INTEGRAL Data Analysis [6], which describes how to get started with the ISDC software. To install the entire software package users will need documents [5] and [7]. All these documents, and many more besides, are available from the ISDC Software Download Page:

`http://isdc.unige.ch/index.cgi?Soft+download`

Users wishing to use the JEM–X Science Analysis software will need the JEM–X Analysis Users Manual [2]. The previous scientific validation report with the software in OSA 3.0 is presented in the JEM–X Scientific Validation Report [4].

For a complete description of the inner workings of the JEM–X software, users are referred to the JEM–X ISSW ADD [1]. The ADD is a detailed description of the software intended for

developpers at ISDC and within SDAST. It is in no way required for understanding the JEM–X scientific analysis but is useful when the user wants to set specific parameters.

A full description of the JEM–X instrument can be found in the JEM–X Instrument User Manual [8] and the Experiment Interface Document part B [9]. However, the details of the instruments contained in these documents are not needed to run the science analysis — though an acquaintance of the basic working of the instruments is helpful.

Bibliography

[1] Instrument Specific Software for JEM–X: Architectural Design Document. Version 9.0, June 2004 (retrieve ISDC Tech).

[2] JEM–X Analysis User Manual (OSA-UM-JEMX). Version 3.0, December 8, 2003 (retrieve ISDC Software).

[3] JEM–X Observer's Manual (INT-SOC-DOC-023). Issue 2, June 30, 2004 (retrieve ESA).

[4] Instrument Specific Software for JEM–X: Scientific Validation Report. Version 3.0, December 5, 2003 (retrieve ISDC Software).

[5] Installation Guide for the INTEGRAL Science Analysis System. Version 1.4, December 8, 2003 (retrieve ISDC Software).

[6] Introduction to the INTEGRAL Data Analysis. Version 3.0, December 8, 2003 (retrieve ISDC Software).

[7] ISDC Data Repository Organisation. Version 1.14, September 3, 2002 (retrieve ISDC Software).

[8] JEM–X Instrument User Manual. Version 6.0, March 1, 2004 (retrieve DSRI).

[9] JEM–X Experiment Interface Document, Part B. Version 5.6, March 8, 2002 (retrieve DSRI).

ISDC Tech ISDC homepage → Documents → ISDC Tech

ISDC Software ISDC homepage → Software → Download → "Doc Tree" in "INTEGRAL Offline Scientific Analysis version 3.0"

DSRI DSRI homepage → Astrophysics → JEMX → Documents

1.3 Acronyms and Abbreviations

ADD Architectural Design Document

DSRI Danish Space Research Institute

EIDB Experiment Interface Document, part B

FOV Field of view

GACE Grupo de Astronomía y Ciencias del Espacio

IDAS_SW INTEGRAL Data Analysis System Software

INTEGRAL International Gamma-Ray Astronomical Laboratory

IROS Iterative Removal Of Sources

ISDC INTEGRAL Science Data Centre

ISSW Instrument Specific Software

JEM–X Joint European Monitor for X-rays

OSA Offline Scientific Analysis software

PVPhase Performance Verification Phase

SDAST Science Data Analysis Software Team

Chapter 2

Data correction

Prior to using the individual data events to make images, spectra and lightcurves various conversions and corrections have to be performed. Though these are not scientific data products, it is of fundamental importance that these corrections are performed properly.

2.1 Energy calibration

The energy calibration of the JEM–X units is based on the built-in radioactive sources (four in each detector) that track the time dependence of the gain. Each such calibration spectrum is acquired in a period of 256 seconds and is transmitted in the house-keeping data.

The spatial variations of the gain has been measured during preflight calibration at Ferrara University, Italy, and they are shown in Figures 2.1 and 2.2.

The detector gas is mostly xenon and it means that Xe fluorescence photons with an energy of 30 keV are produced everywhere in the detector volume. This line can be used for calibration purposes.

By collecting data from each anode strip (or rather with a given coordinate – raw x – perpendicular to the strips) an inflight energy calibration has been obtained that improves the energy correction somewhat. Figures 2.3 and 2.4 show the relative correction factors.

Figure 2.5 shows the effect on the full detector spectrum of JEM–X1 of correcting first for time and spatial variations, and then of correcting for each anode strip separately. A clear improvement is seen in the energy resolution of the instrument. The right-most peak in this figure is the Xe fluorescence line seen during an empty field observation. Clearly the spatial (SPAG) correction provides the greatest improvement in energy resolution over the raw spectrum, but a small extra improvement in energy resolution has been obtained by the introduction of the anode-by-anode correction.

Similar results are seen for JEM–X2 in figure 2.6, though a somewhat smaller improvement in energy resolution seems to occur with the inclusion of dead anode corrections. We can however, clearly see that the overall gain of JEM–X1 is substantially lower than that of JEM–X2. The JEM–X1 spectrum differs from that of the JEM–X2 by the addition of a strong ^{55}Fe line at 6 keV that originates from the two ^{55}Fe calibration sources which produce quite a few events that spill out of the calibration areas. Both units show similar spillover events from the ^{109}Cd sources that produce a doublet at 22/25 keV, though JEM–X2 naturally has a stronger ^{109}Cd feature than does JEM–X1. Since the linearised energy channels shown in figures 2.5 and 2.6 do not correspond to energy channels used in the ISDC software, it can be seen that the two JEM–X units have markedly different gain factors.

The background spectra where these corrections have been applied are shown in figures 2.5 and 2.6. Two distinct inflight energy calibration periods have been used for each instrument to take account of the possible evolution of the actual dead and sick anodes list. This shows that, while no difference occurs for JEM-X1 (fig. 2.5) during more than one year of inactivity (apart from a few days activation), a marginal effect is visible for JEM-X2 (fig. 2.6) after a four month activity period.

The calibration spectra are recorded in a 256 s interval. There are four spectra per JEM–X unit. The peak position and width is determined for each and stored in a table. Figure 2.7 illustrates the short term gain development of anode section 3 in JEM–X2 during revolutions 87 through 90 where the satellite is eclipsed around perigee and therefore cools down. The heating shows as a gain increase upon turn-on of the instrument. The gain correction is determined as a reasonably smooth fit to the measured gain values (also shown in the figure).

The presence of glitches i.e. short, sudden gain decreases of the gain is shown by the data points lying below the general trend. These glitches happen very locally on the detector (perhaps induced by cosmic ray particles) and cannot be corrected for. The two spikes above the common level are caused by emergency switch offs and when the instrument is switched on again the gain starts at a high level but relaxes in half an hour.

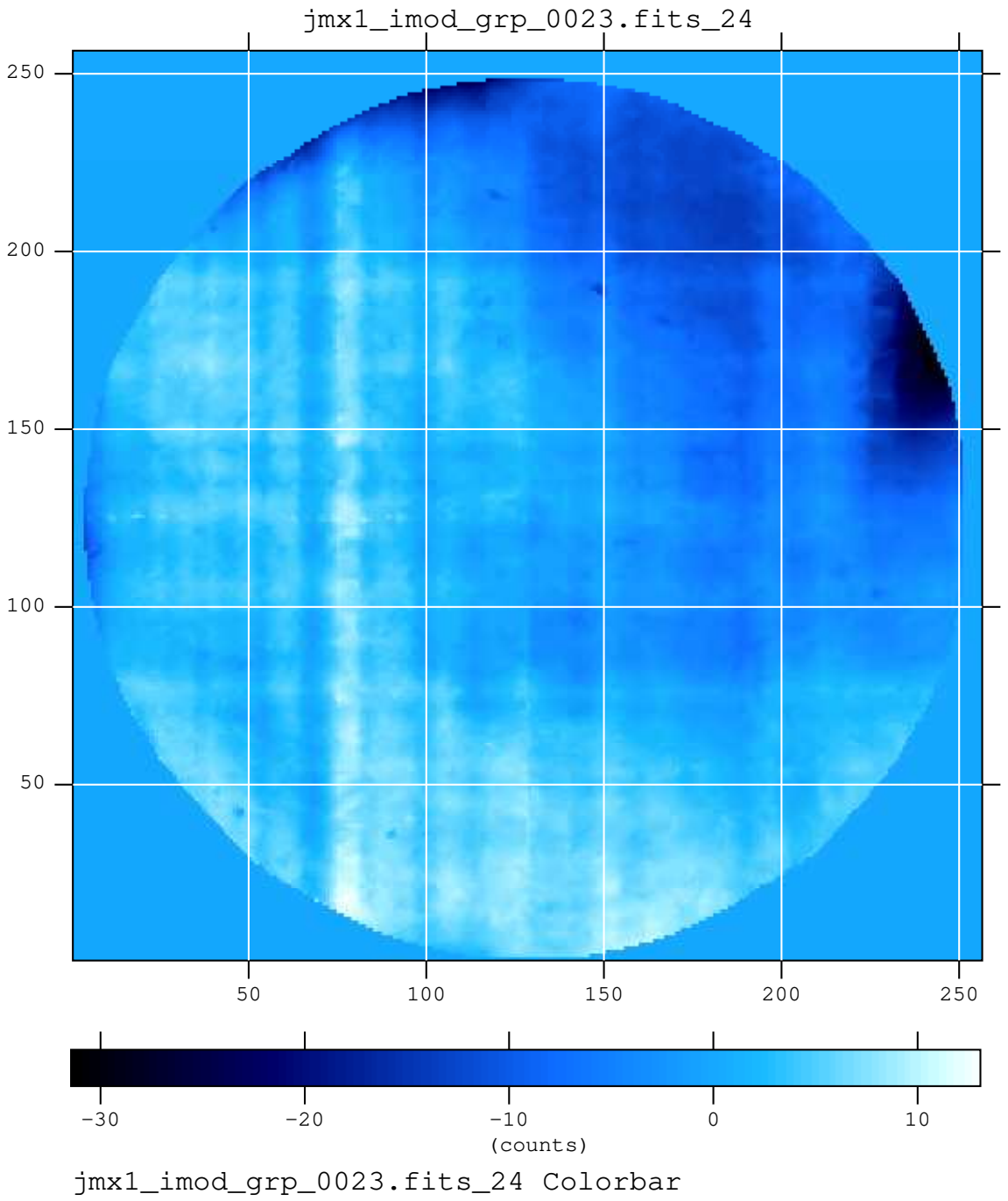

Figure 2.1: Spatial gain variation of JEM–X1 given in percents from the average.

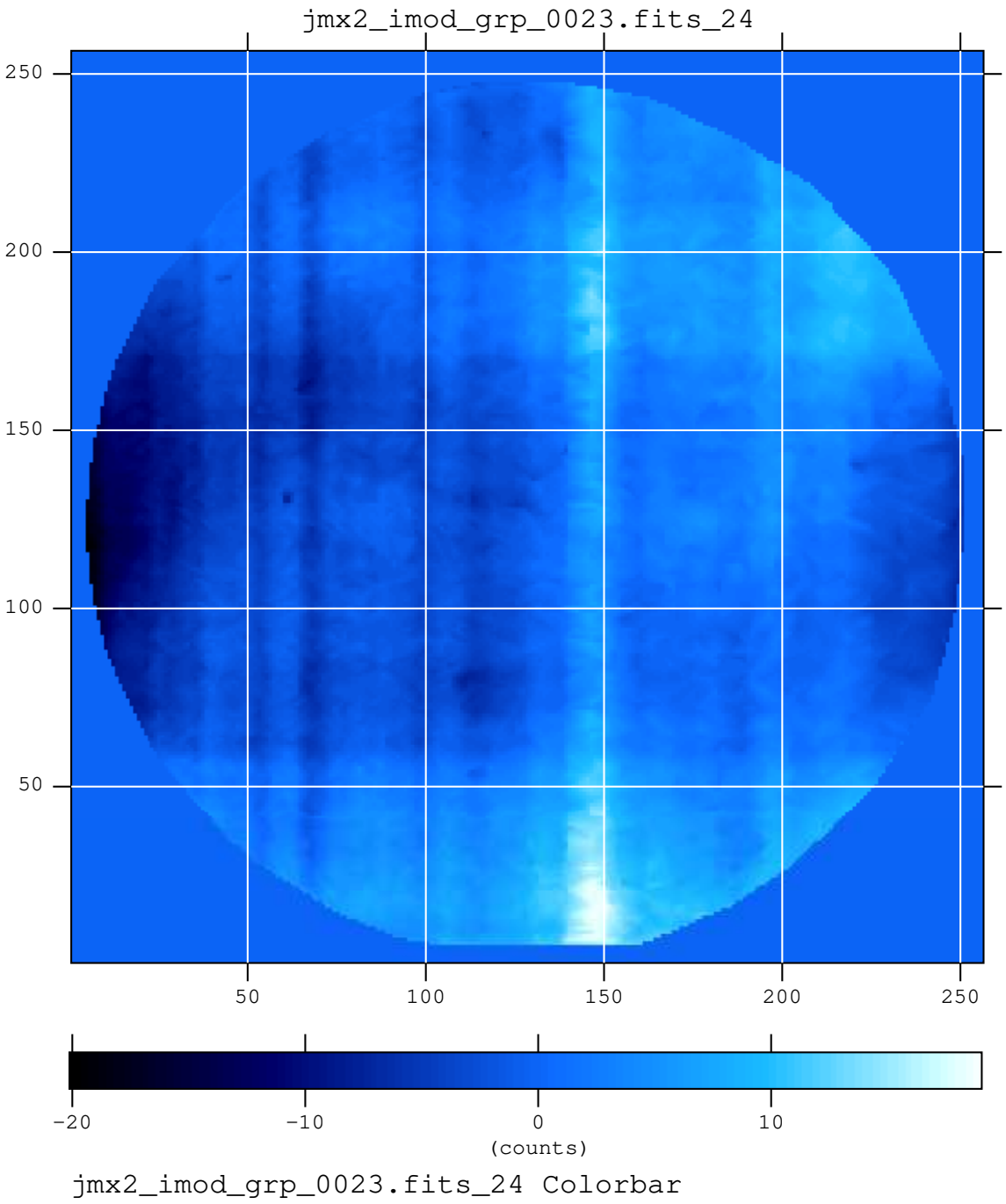

Figure 2.2: Spatial gain variation of JEM–X2 given in percents from the average.

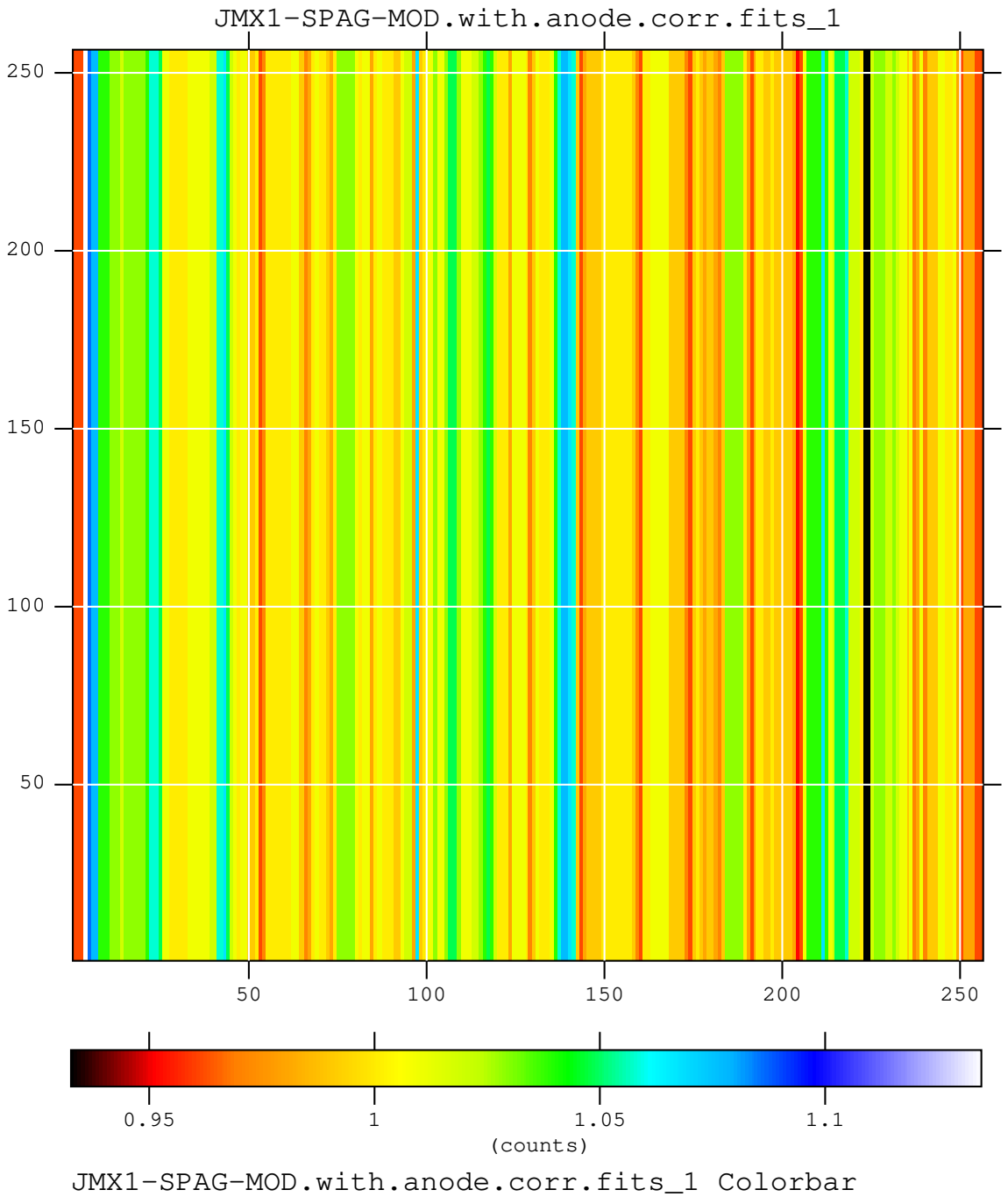

Figure 2.3: Spatial gain variation of JEM–X1 for individual anodes, expressed as factor relative to the mean.

DANISH NATIONAL SPACE CENTER

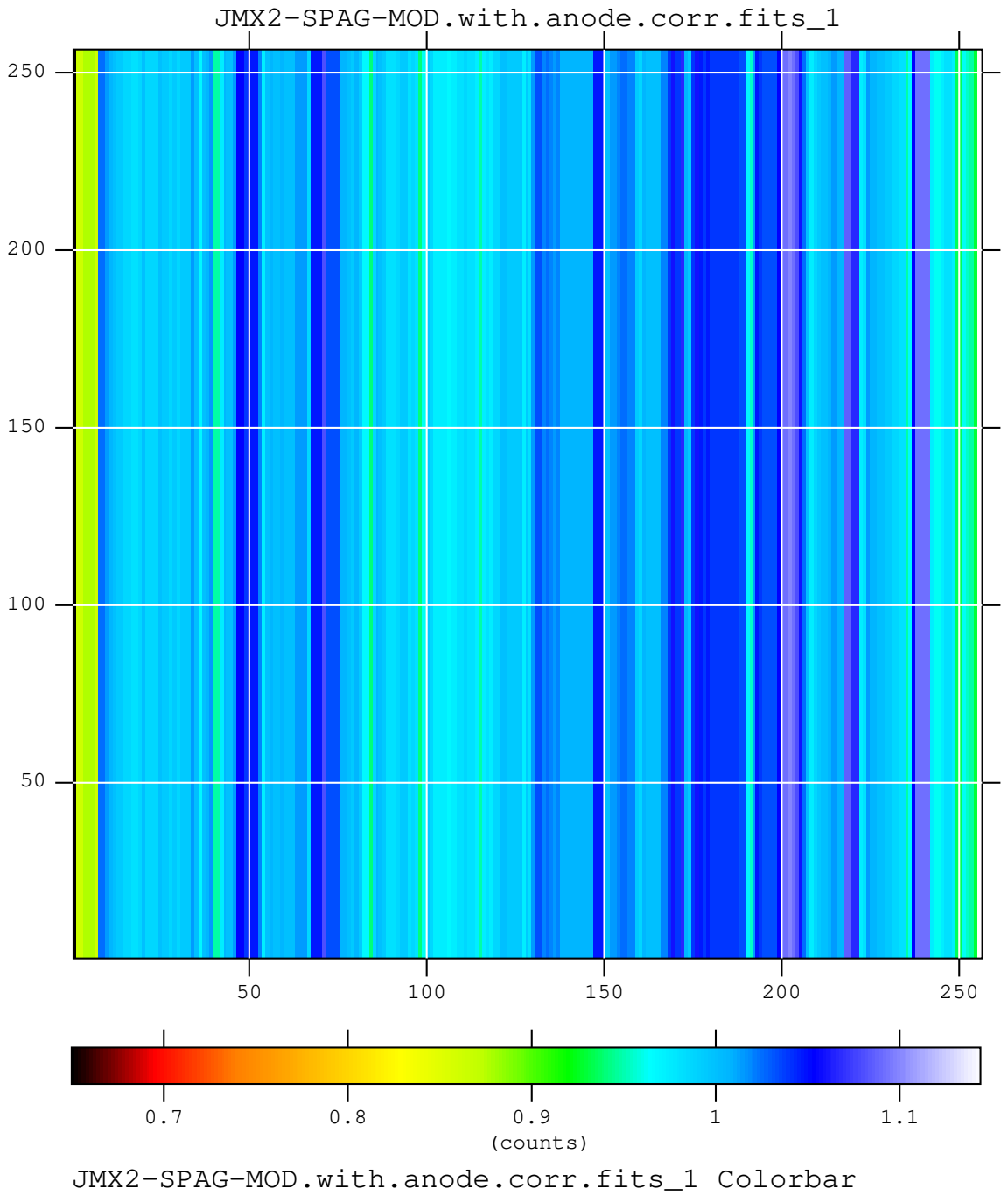

Figure 2.4: Spatial gain variation of JEM–X2 for individual anodes, expressed as factor relative to the mean.

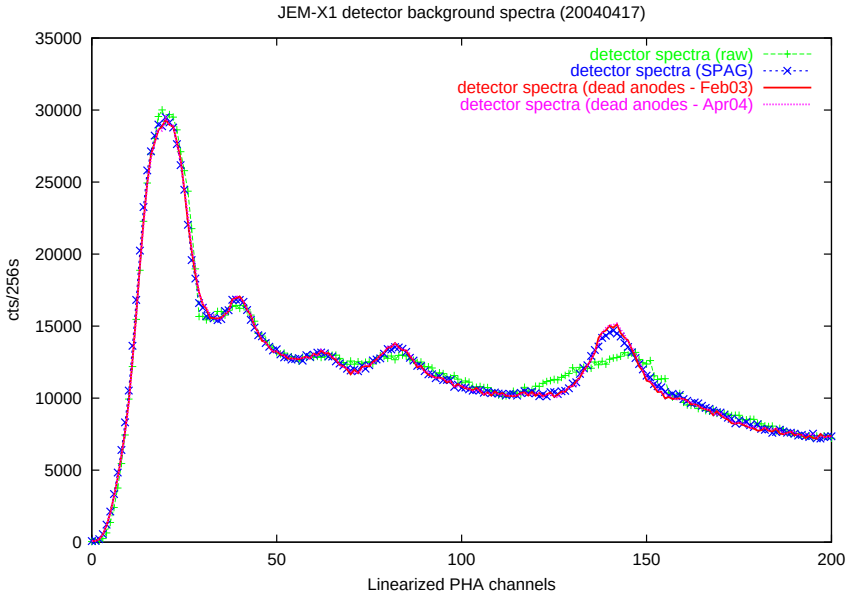

Figure 2.5: Spectrum of JEM–X1 with spatial and anode corrections. The energy scale used here does not relate to any scale produced by the ISDC software, but is simply a linearised scale based on PHA values.

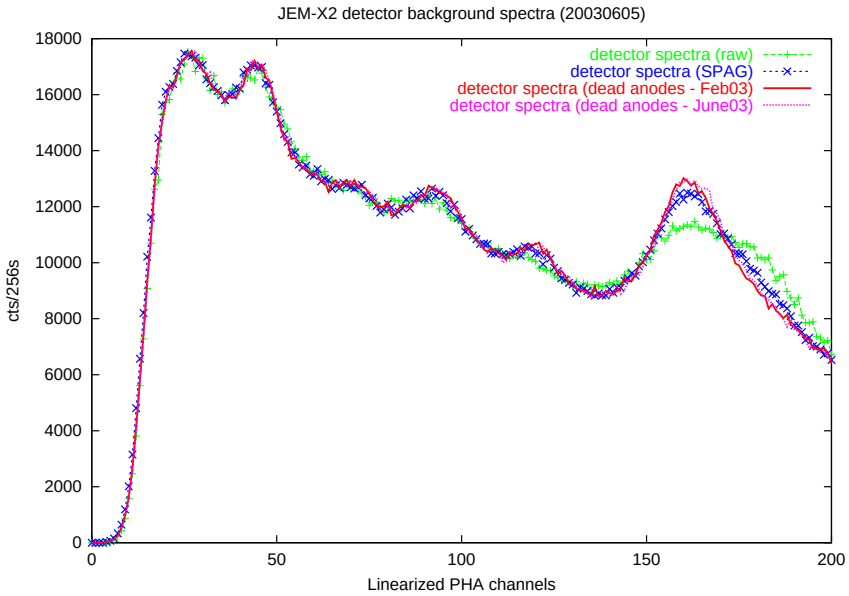

Figure 2.6: Spectrum of JEM–X2 with spatial and anode corrections. The energy scale used here does not relate to any scale produced by the ISDC software, but is simply a linearised scale based on PHA values.

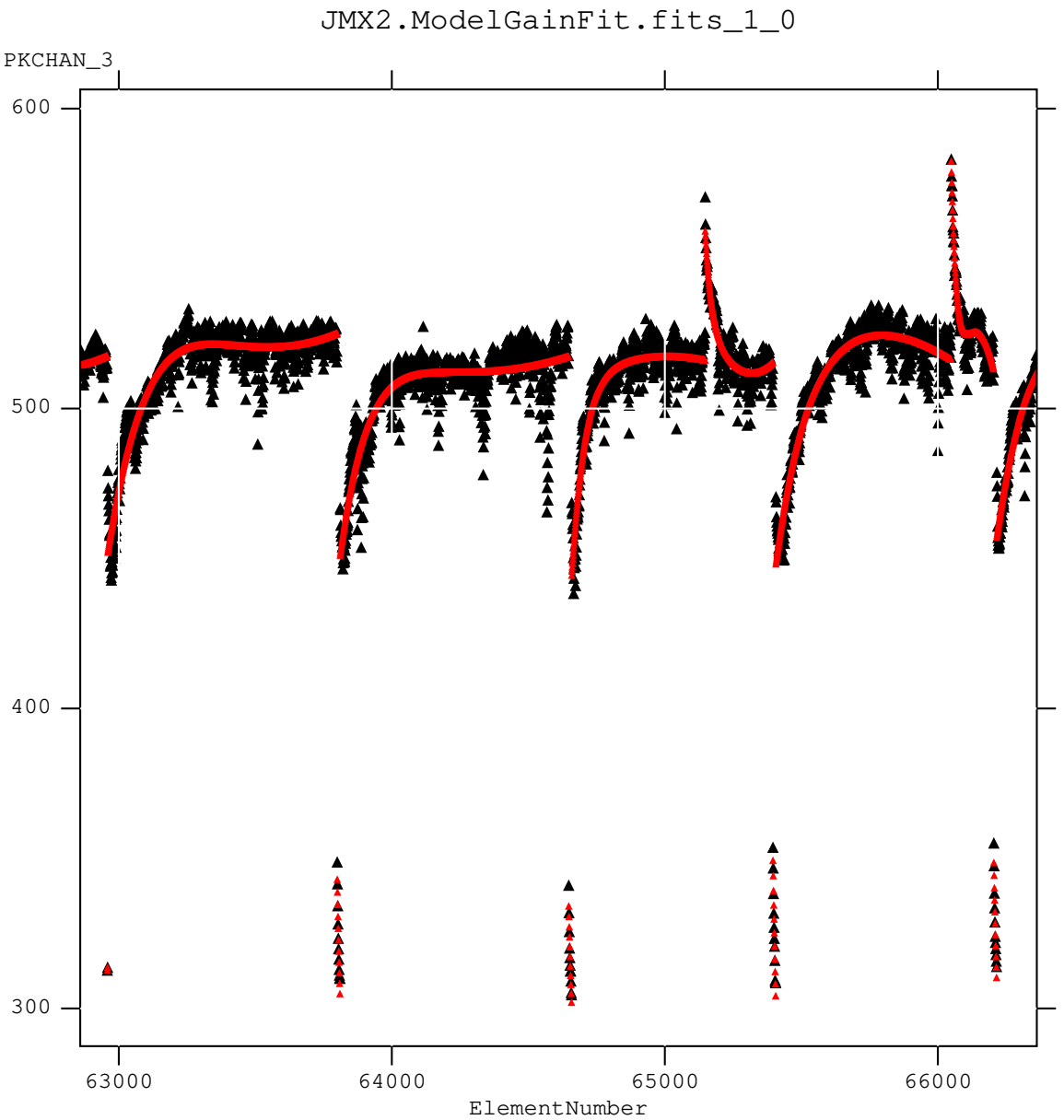

Figure 2.7: Gain for JEM–X2 anode section 3 in rev. 87–90 per 256 s interval.

2.2 Evolution of gain

After a couple of months in orbit it became apparent that the detector gain was steadily increasing for the JEM–X unit in operation. This has been counteracted by reducing the high voltage at about 6 weeks interval. This can only be done in steps.

The situation for JEM–X1 is shown in Figure 2.8. JEM–X1 was shut down from revolution 45 to 170 with the exception of a Crab calibration in revolution 102. In the earliest revolutions there is a clear gain increase, which seems to decrease with time despite the constant HV value and this seems to have stopped by revolutions 39 to 45. The revolution 102 data suggests a gain increase for both the cadmium and the Fe sources. The reason for this is unknown.

Figure 2.9 with the data for JEMX–X2 demonstrates that the gain increase affects all four calibration sources in the same way and hence probably also the entire detector plate. We can also see that the rate of increase is related to the level of the high voltage supply on the plate. The gain increases more slowly as the HV is decreased.

2.3 Evolution of energy resolution

The expected energy resolution is $\Delta E/E = 0.47/\sqrt{(E_{\mathrm{keV}})}$. For the Xe line this would give a FWHM of about 2.6 keV (9%).

The presence of glitches (see p. 8) with shorter timescales than can be corrected for, as well as the dead or weak anodes, reduce the resolution somewhat as illustrated in Figures 2.10 and 2.11 that show the time development. Spectra on a science window timescale from the whole detector surface and with standard energy corrections have been used for this analysis. As already suggested by figures 2.5 and 2.6, the average relative resolution of the Xe line has remained quite stable around 9% for JEM-X1, while JEM-X2 exhibits a slow degradation from 9% to about 14%.

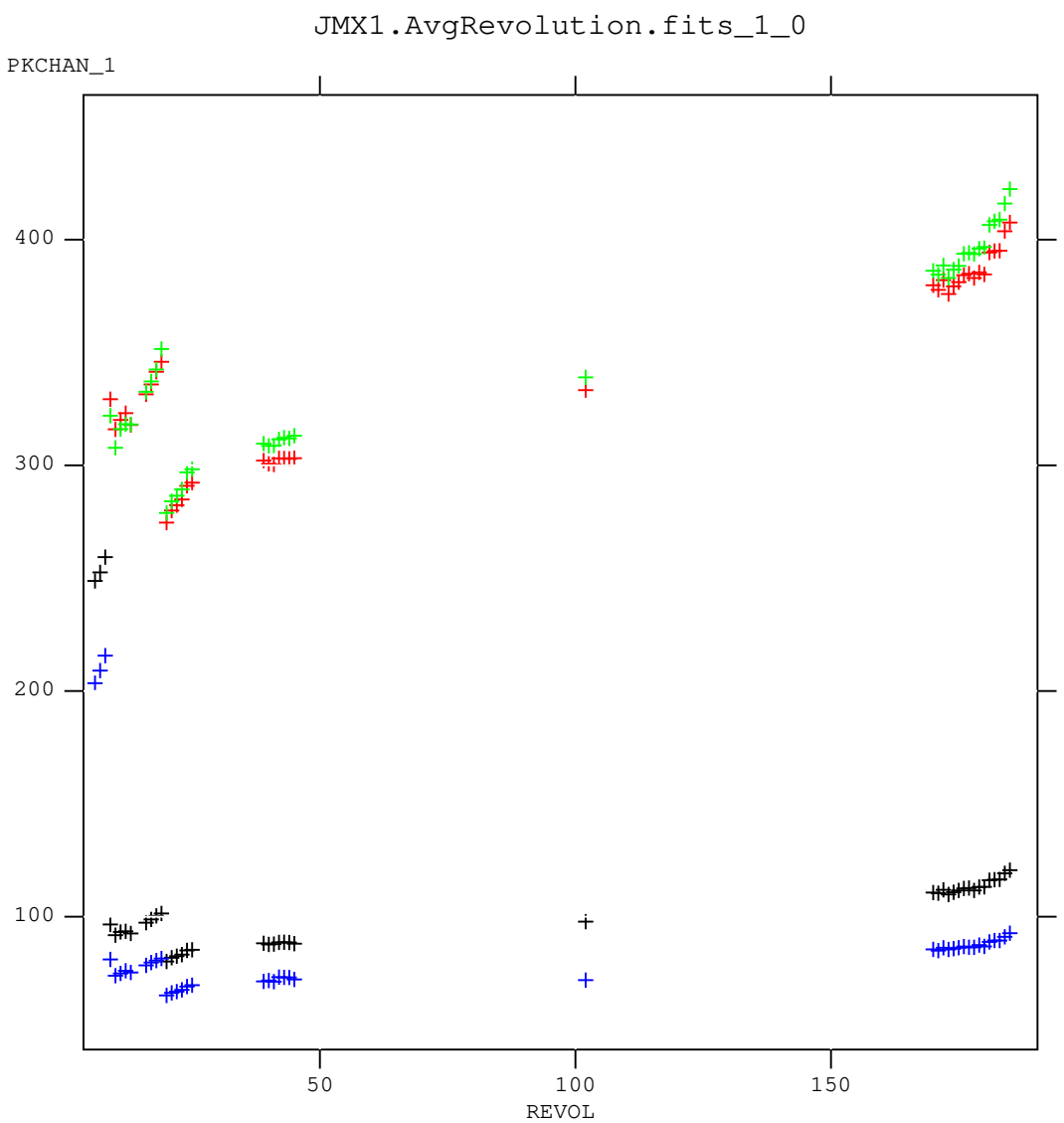

Figure 2.8: Shows the onboard peak channels for the four calibration sources of JEM–X1. Black is source 1 (^{55}Fe, 6 keV); red is source 2 (^{109}Cd, 22 keV); blue is source 3 (^{109}Fe, 6 keV); green is source 4 (^{109}Cd, 22 keV).

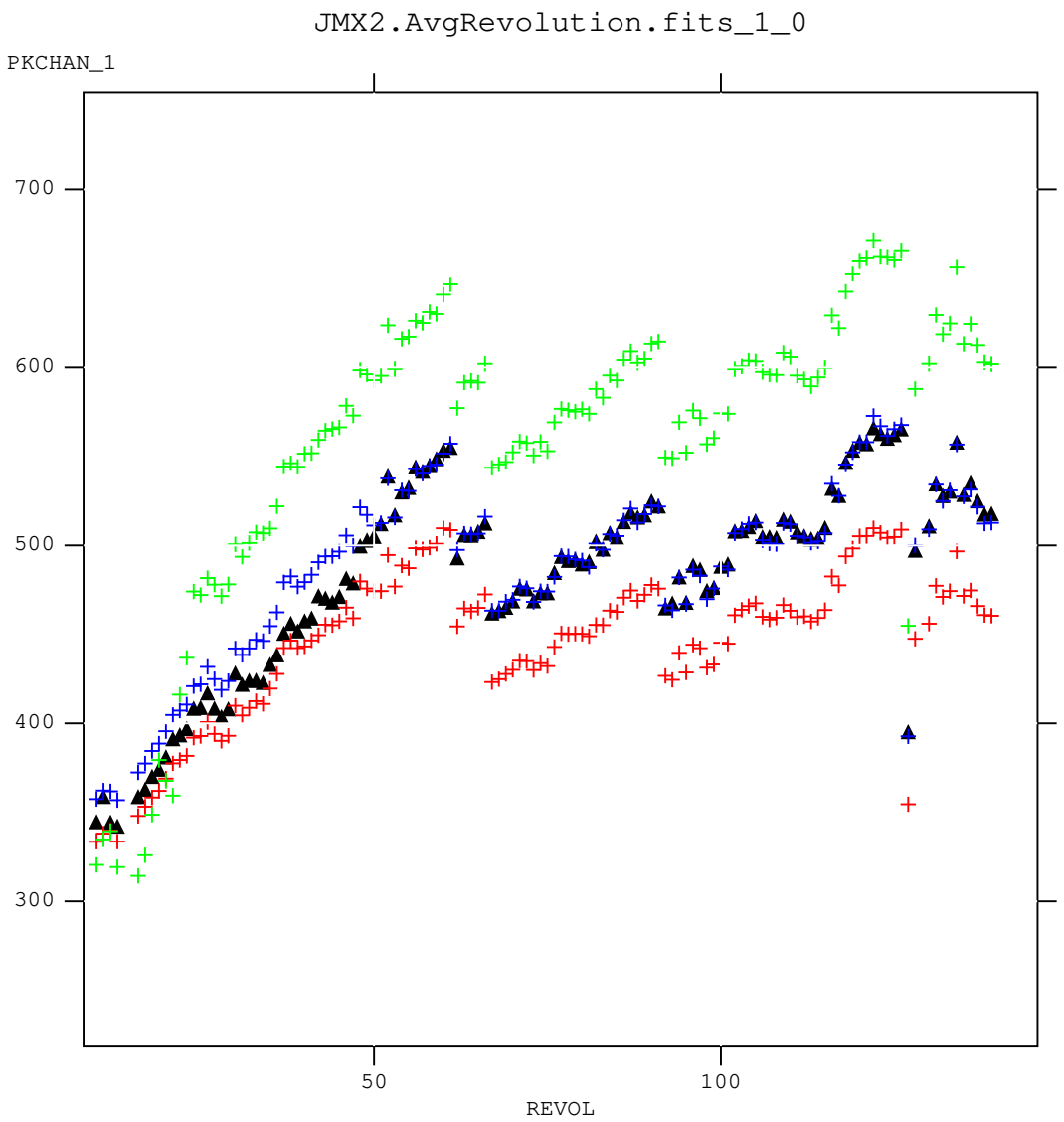

Figure 2.9: Shows the value of the onboard energy channel of the peak of the ^{109}Cd 22 keV lines for the four calibration spectra used in JEM–X2. Black is source 1; red is source 2; blue is source 3; green is source 4. The steady increase in detector gain is clearly apparent. The sudden drops in peak channel value show where the high voltage supply to the microstrip plate has been lowered to keep the gain within the range used for pre-flight calibration.

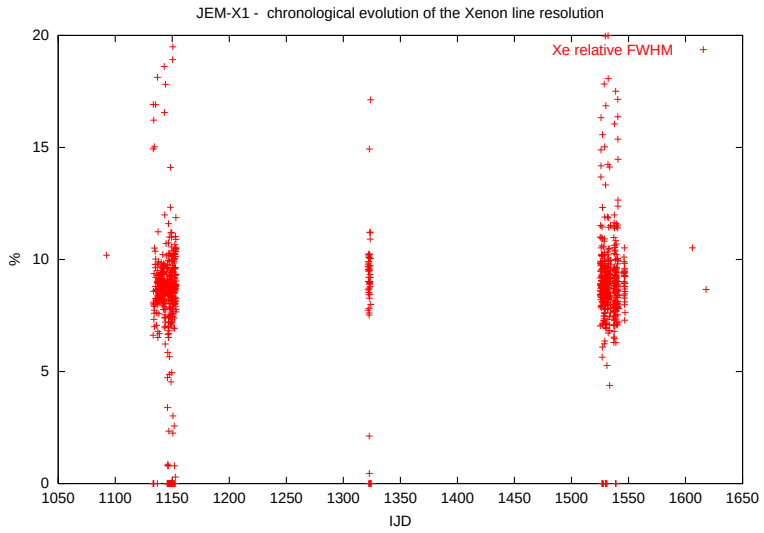

Figure 2.10: The evolution of the energy resolution of JEM–X1 for the 30 keV Xe line as determined from the detector spectra per science window.

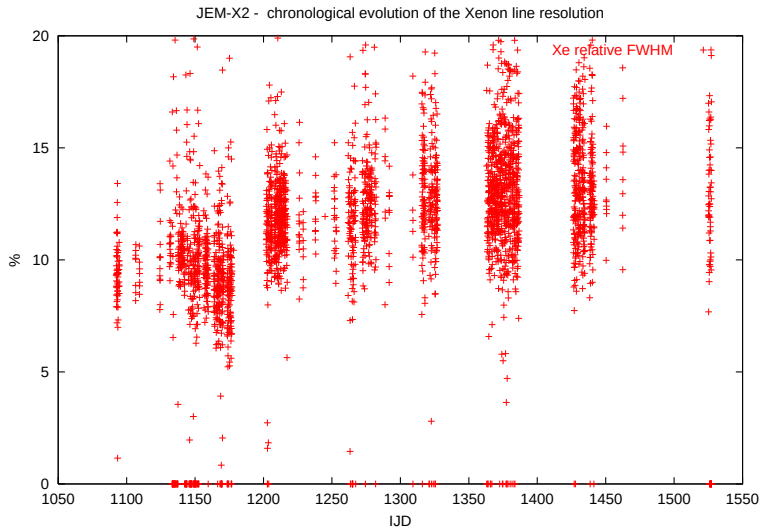

Figure 2.11: The evolution of the energy resolution of JEM–X2 for the 30 keV Xe line as determined from the detector spectra per science window. The apparent decrease between IJD 1125 and IJD 1175 is an artefact due to a temporary modification of the high energy cutoff of the instrument.

2.4 Dead time and grey filter

The deadtime corrections for JEM-X data are derived from the HK data. The corrections have been derived during ground testing and are based on the measured execution times for the various branches of the event processing. Deviations from the algorithm used, due to non-linear effects, are only expected for very bright sources (several Crab units).

The method that is now used for dead time determination is to read all the different event classification counters in the housekeeping packets, and from these find: input dead time, effective dead time due to grey filter loss and effective dead time due to buffer loss. Buffer loss occurs when buffers are too full to take more data or get flushed. The housekeeping packets stored in JMXi-CSSW-HRW list such event counters as: events accepted for processing; events rejected by grey filter; events rejected by various particle rejection criteria and events accepted for transmission in telemetry. Each type of processing has an associated dead time which can then be added up.

Fluxes and countrates must be corrected for the effect of the grey filter since the fraction of detected events appearing in the telemetry is equal to $(G + 1)/32$, where G is the value of the grey filter.

Figure 2.12 shows how input dead time decreases as the grey filter mechanism kicks in and gradually increases in effect. Input dead time decreases because events rejected by the grey filter mechanism are processed very rapidly with little data read in. However, the combined dead time and grey filter correction of the instrument increases greatly with increased grey filtering. No buffer loss is evident in this data at all. The grey filter value begins at 31 (full transmission) for the first half of the figure and gradually falls to 21 (69% transmission).

Currently flux and countrate corrections are performed on the basis of the input dead time derived from the housekeeping data with 8 s time resolution, plus grey filter corrections based on the instrument status table (JMXi-INST-STA) grey filter values which have a time resolution equal to that of the rate at which the onboard software can change the grey filter. In the future any dead time due to buffer loss will also be included in the correction with 8 s resolution (see below). However, even without buffer loss included, we are confident that the wide variation we see in flux determination (see section 6.3) is due almost entirely to vignetting uncertainties and not to any problems with the dead time correction. Once buffer loss is in place we believe that this correction will be done as well as it can within the limits of the time resolution of the housekeeping. For more detailed dead time analysis (e.g. millisecond pulsars), users will have to do their own offline analysis.

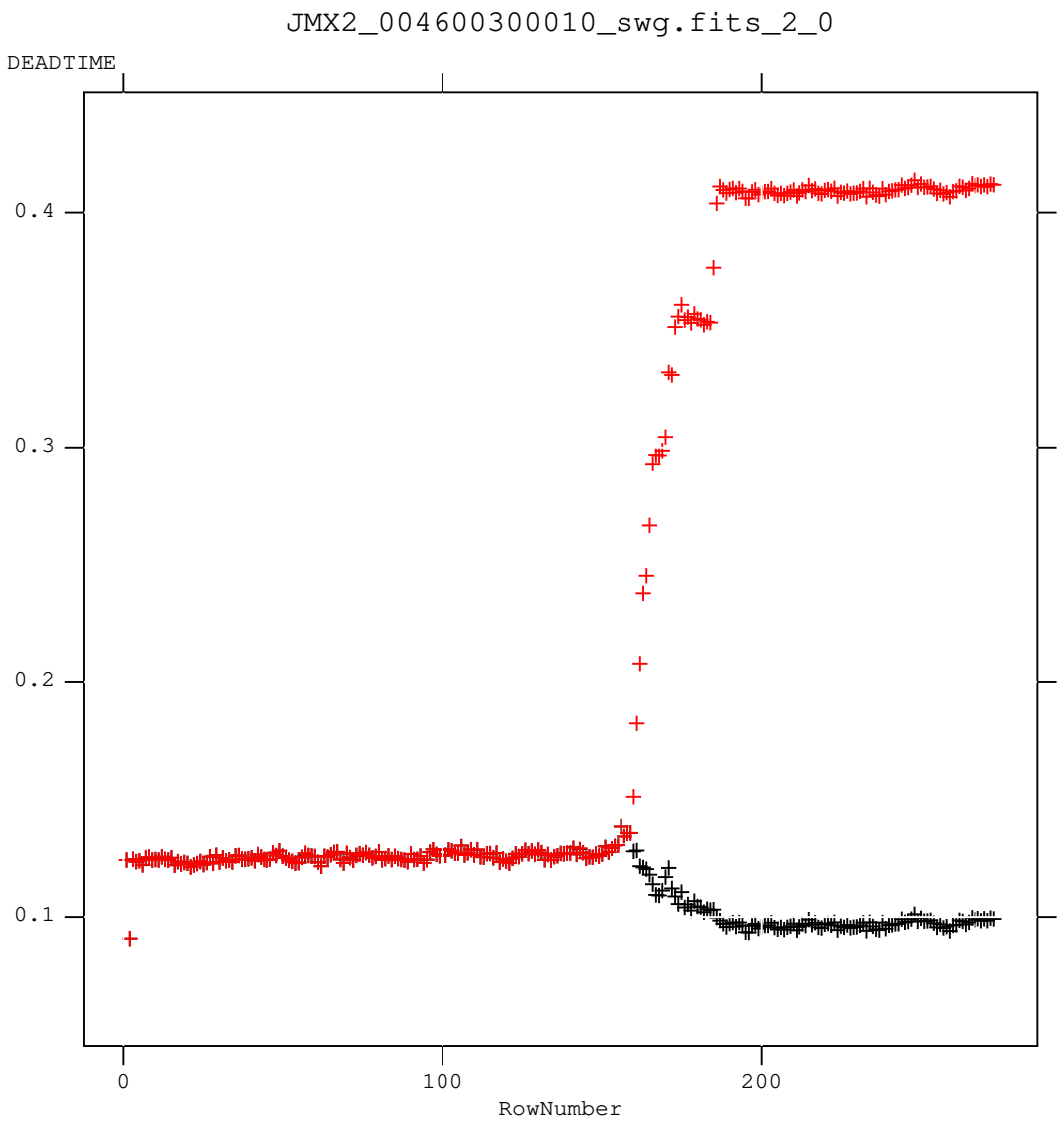

Figure 2.12: Typical dead time behaviour of JEM–X2 with grey filtering. Red line shows total dead time and grey filter corrections. Black line shows instrument dead time only

N.B. Data points are spaced 8 seconds apart

2.5 Timing

2.5.1 Absolute timing

The finest time resolution of JEM–X is 122 micro-seconds, in the sense of the width of the smallest time bin. The phase of this time bin is known relative to the INTEGRAL onboard time with an accuracy of a few micro-seconds. The absolute timing accuracy relative to UTC is determined by the the INTEGRAL time relation (Walter et al.). The studies of the Crab pulsar (Brandt et al., Kuiper et al.) show the absolute timing to be better than 100 micro-seconds.

References:
Brandt, S. et al., A&A 411, L433, 2003
Kuiper, L. et al., A&A 411, L31, 2003
Walter, R. et al., A&A 411, L25, 2003

2.5.2 Relative timing

This section serves as a warning against the possible detection of QPO type features around 1300 Hz in JEM–X data at the lowest energies. JEM–X is currently working at a significantly lower gain than originally planned and for which the onboard electronics were designed. This means that the low energy theshold is partly determined by an electronic cut-off and not entirely by the transmission of the Be window. A side effect is that the sensitivity to low energy photons weakly depends on the time from the previous event trigger (including particles) with a period around 0.77 ms, corresponding to an incoherent frequency around 1300 Hz. The effect will be strongest for the very brightest and softest sources. The details of this "feature" are under investigation.

2.6 Event quality filtering

Each event is tagged with a status flag (column "STATUS" in jmxi_full_cor.fits) (see [1]) that describes the quality of the energy and position assignment.

The following table is an example from SWID 013700170010 (JEM–X2) where 67801 events were recorded, to show the frequency of the various status values.

STATUS	Description	Number of events	Fraction
0	OK	58023	85.33%
4	On dead anode in FRSS	0	
8	Bad time correlation	0	
16	Bad anode	3955	5.81%
64	Poor gain history	1503	2.21%
128	Bad energy	0	
256	Bad X position	0	
512	Bad Y position	0	
1024	FRSS leak	299	0.44%
2048	Occurred before SETUP	232	0.34%
4096	Outside nominal area	1385	2.04%
8192	From hot spot	23	0.03%
16384	Next to bad anode	2578	3.79%

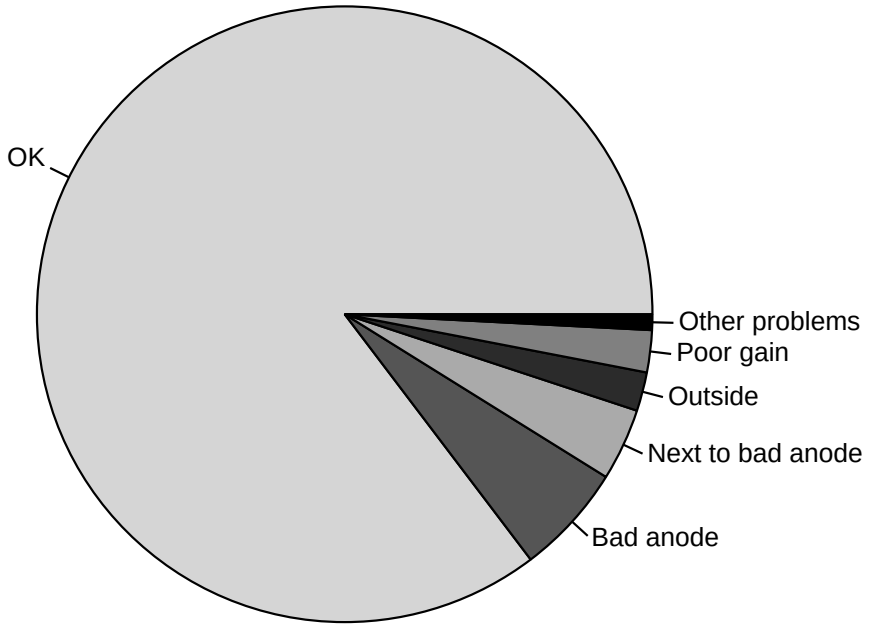

Figure 2.13: Distribution of event STATUS values. Problem cases with a fraction below 1% are summarized as “other problems” in the chart.

Chapter 3

Background determination

One of the most intricate tasks that has to be done prior to image deconvolution, is to determine the fraction of counts that come from astronomical sources and those that are due to other effects such as particle interactions inside and close to the detector. The onboard software does fairly rigorous tests on the many detector signals that describe each detected event to eliminate those which have characteristics expected of cosmic ray particles. There is a small fraction of these that are mis-interpreted as photons and therefore contribute to the instrument background. On top of that there are two classes of x-ray photons that also complicate the source imaging and detection procedures:

Diffuse X-rays Photons from non-resolved or very extended X-ray sources. These photons are modulated by the mask pattern and found over the entire detector area.

Instrument background Bremsstrahlung photons produced by interaction of cosmic rays with the materials of the satellite around the instruments. These photons are mainly found around the edge of the detector and have no mask pattern modulation.

Figure 3.1 shows the detector shadowgram of JEMX–X2 from a blank field observation in revolution 41. One of the most striking features of this detector image are the dark stripes running vertically across the detector. These are 'dead' anodes and their affected neighbours that produce far fewer event counts than undamaged anodes.

The effect of instrument background is clearly seen around the detector rim as an excess of event counts, which also happen to be strongest at each side of the detector where the instrument background forms well-defined strips of increased activity. It is not quite clear yet why these two strips occur or why they have such well defined boundaries.

As with the spectrum from the center of the detector, the rim spectra show a very clear peak at 30 keV produced by Xe fluorescence line. However, in contrast to the diffuse background

photons seen in the centre segment spectrum, the rim spectra show a forest of other lines below 30 keV that arise from the many different elements found in the satellite materials surrounding the instrument, however the Xe line is so strong here that it swamps most other lines.

The four black squares at the top of the detector show where the four calibration spectra events have been removed from the scientific data stream for separate processing by the ISDC's Automatic Correction and Calibration (ACC) software. However there are still some background photons that are produced by spillover from the calibration spectra areas. The spectrum integrated over events from these four regions, show as expected strong lines at the ^{109}Cd line at 22 keV, and its smaller component at 25 keV. ^{109}Cd is the isotope used in the four calibration sources. The Xe fluorescence line at 30 keV is also very clear. The 17.4 keV Mo line originating in the collimator is clearly seen all over the detector, as well as the 7.5 and 8.3 keV Ni lines from the calibration source covers. One feature that shows up most clearly in the centre of the detector is the 13.5 keV ^{238}U line.

The background determination software aims to quantify how much of each of these types of spectra is present at each point on the detector, and subtract their contribution from the data before image deconvolution. A library of spectra from different parts of the instrument has been constructed and is included in the calibration files used by the OSA software. There is still a lot of optimization to be done and users may try the analysis with and without background subtraction.

A crude form of background subtraction can be performed by making use of the `radiusLimit` parameter which is a user input parameter. This number indicates the area radius in mm from the centre of the detector that should be used to make imaging shadowgrams. Events further than `radiusLimit` [*unit*: mm] from the centre of the detector are not used in the image deconvolution or source finding processing. This does however mean that all photons, not just background photons, are ignored if they fall close to the detector rim.

Figures 3.2 and 3.3 show the increased background at the rim. A value of about 108 mm for the `radiusLimit` will cut out most instrumental background and calibration spectra overflow.

Subtracting the background may produce a shadowgram with negative pixel values. The image reconstruction copes well with this but the algorithm to match the predicted background shadowgram with the observed shadowgram of all counts is to be improved for later releases in order to avoid subtracting too much.

JEMX−2 background spectrum variations from blank field observation rev. 0041

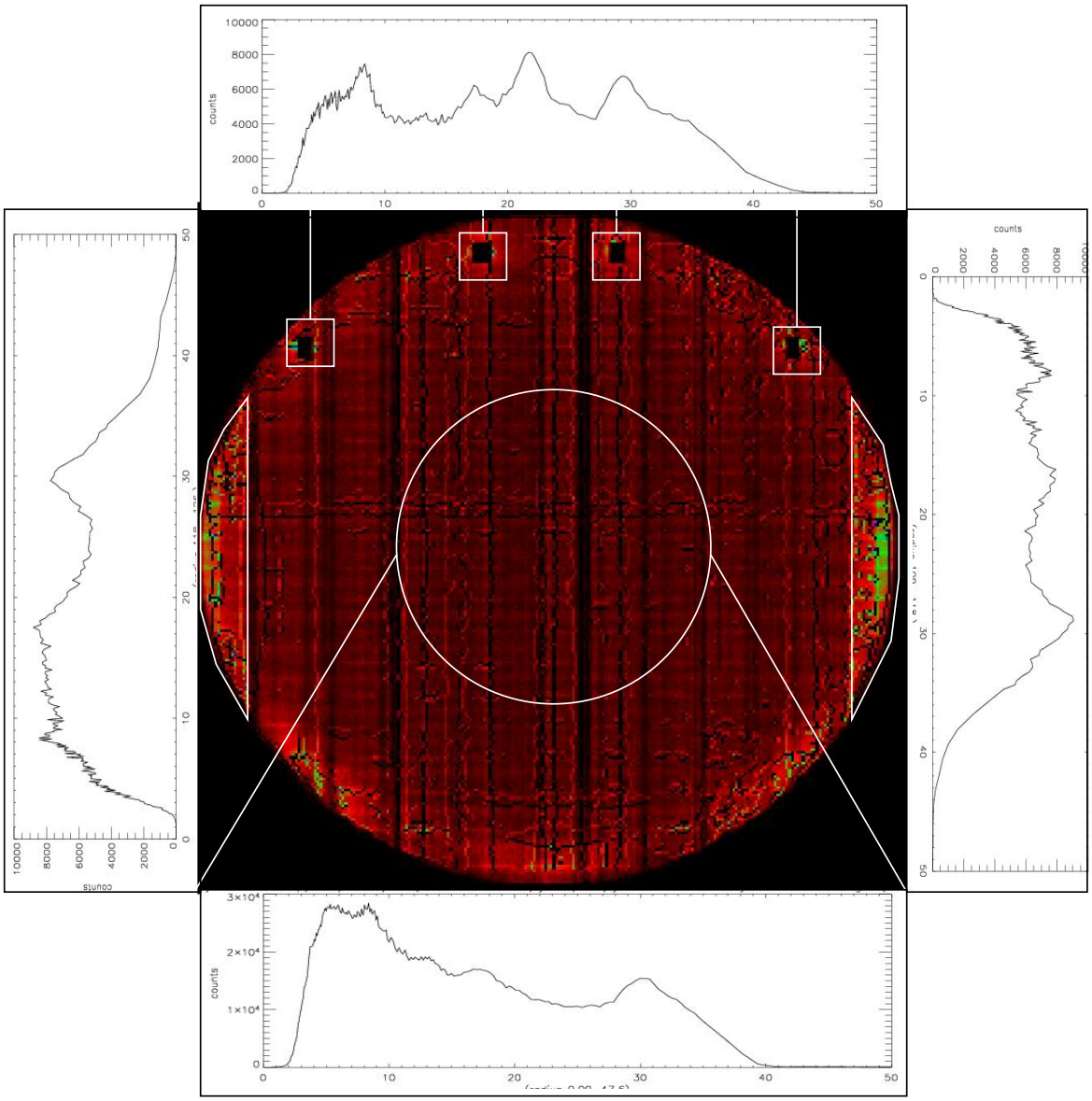

Figure 3.1: Background spectra of JEMX–X2 during revolution 41

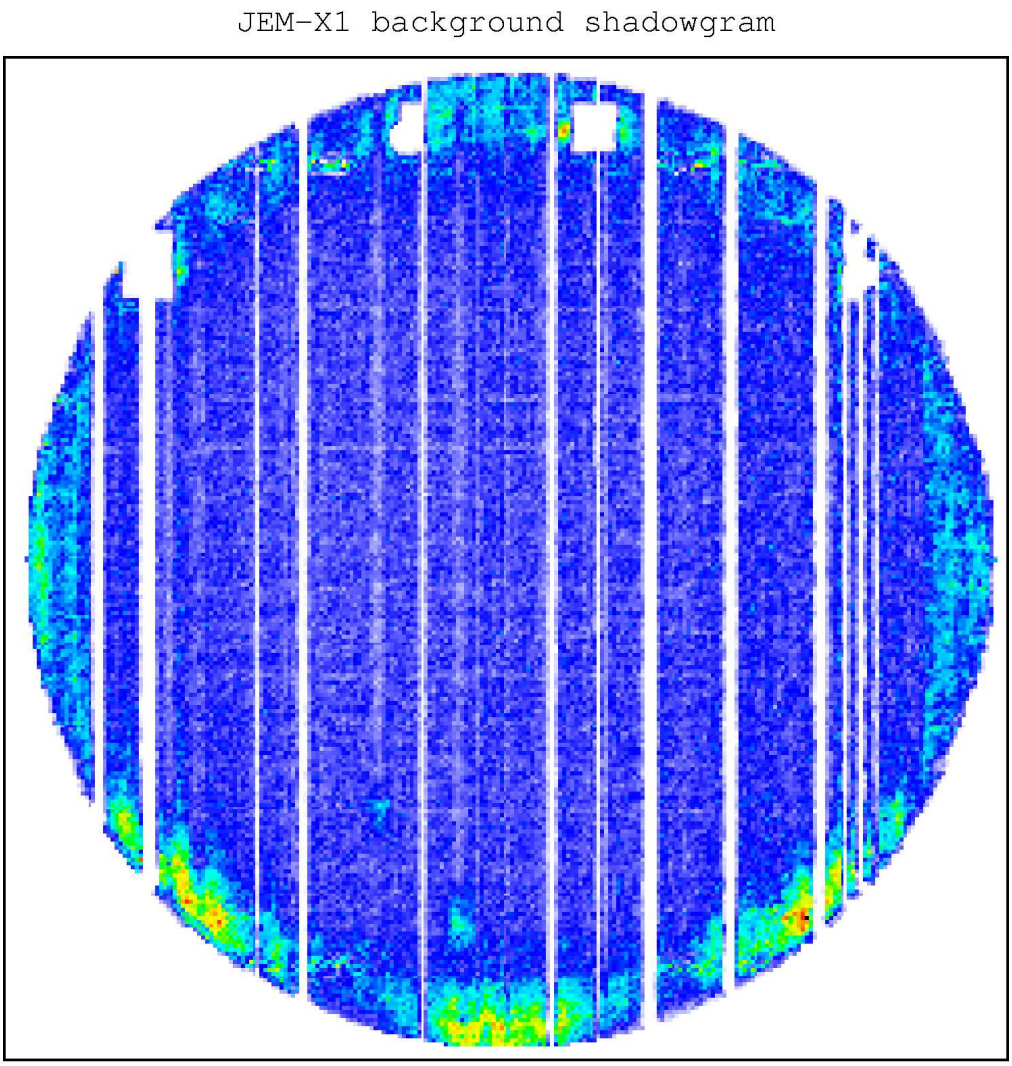

Figure 3.2: JEMX–X1 detector background shadowgram

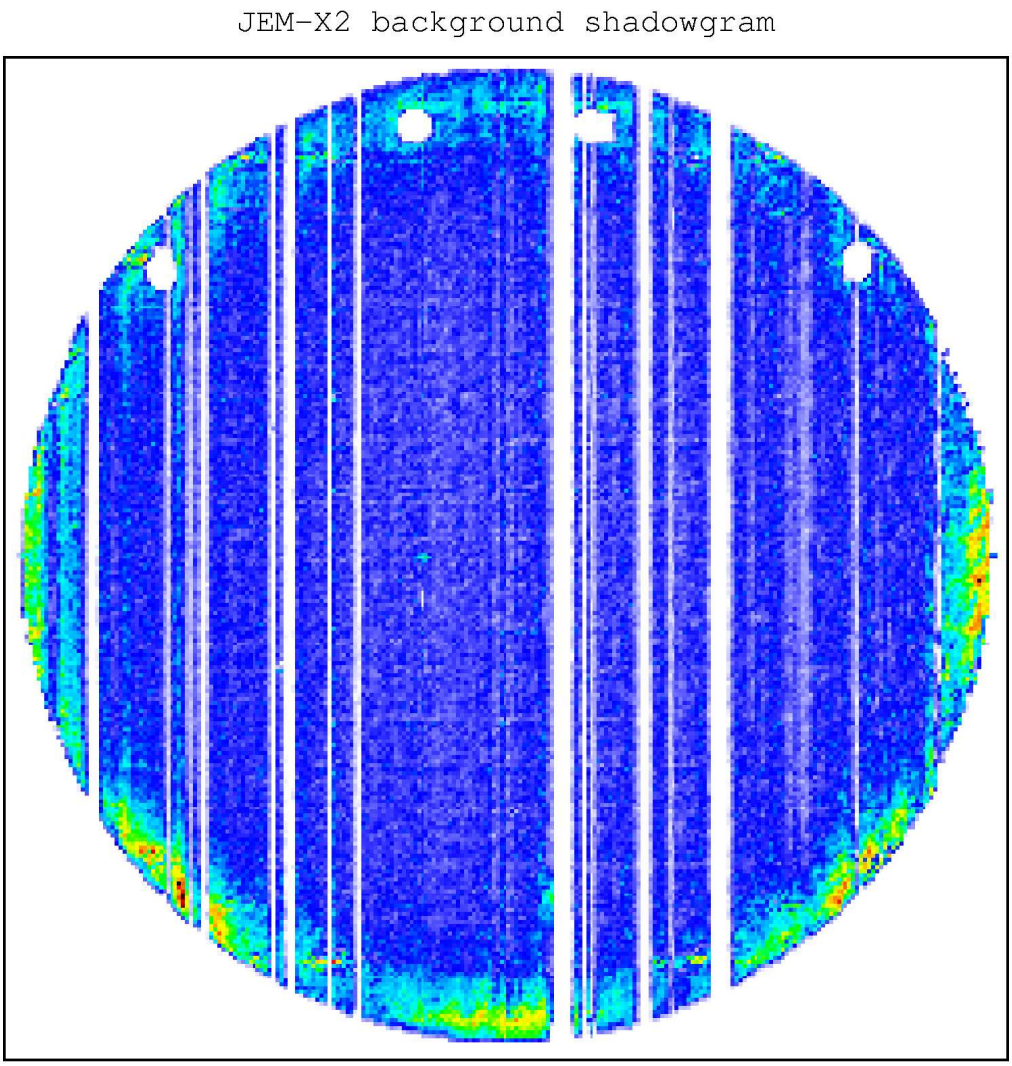

Figure 3.3: JEMX–X2 detector background shadowgram

Chapter 4

Non-imaging results

The OSA software provides a couple of components for binning corrected data from the entire detector into detector spectra and detector lightcurves.

4.1 Detector spectra

As examples the detector spectra extracted from the entire detector and with a radiusLimit of 105 mm are shown in Figures 4.1 and 4.2. They give the usual background intensity and demonstrate that the Xe peak falls at the expected energy.

4.2 Detector light-curves

Some characteristic examples from the beginning of revolution 39 during the Crab calibration are shown in the figures below. The binned data are corrected for deadtime and grey filter effects. The lively grey filter activity during the beginning of revolution 39 is shown in figure 4.3. Four science windows are shown in these three plots with colours black, red (with a data gap), blue and green.

The detector light curve over all energy channels is shown in figure 4.4. It would appear that the grey filter corrections are working satisfactorily since there are no jumps in the light curves where grey filter is changed, though at times of large grey filtering the error bars on the binned data seem to be underestimated. However data bins touching a data gap or at the beginning and end of a science window show large deviations from the rest of the data. The cause of these brief problems still has to be determined.

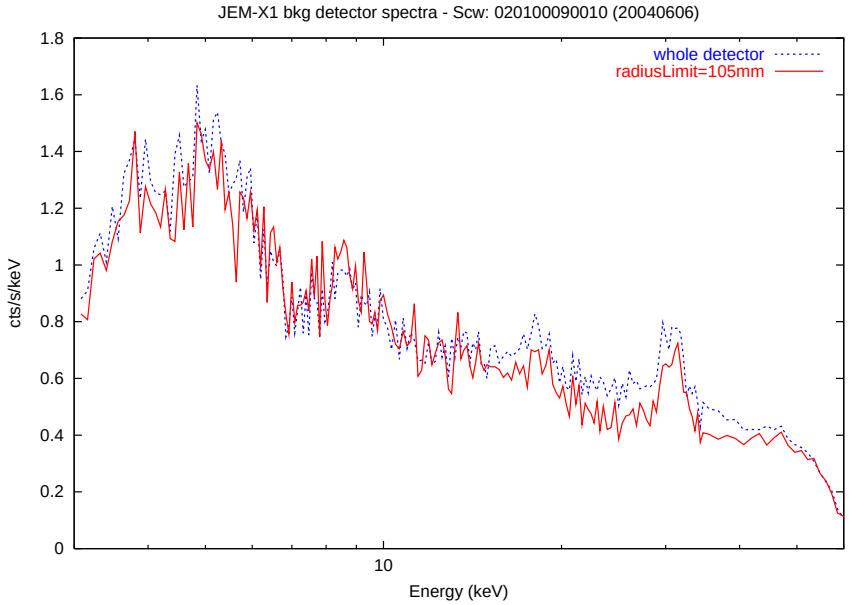

Figure 4.1: JEM–X1 detector spectrum of a blank field observation for a single science window in revolution 122. The Xe line at 30 keV is visible.

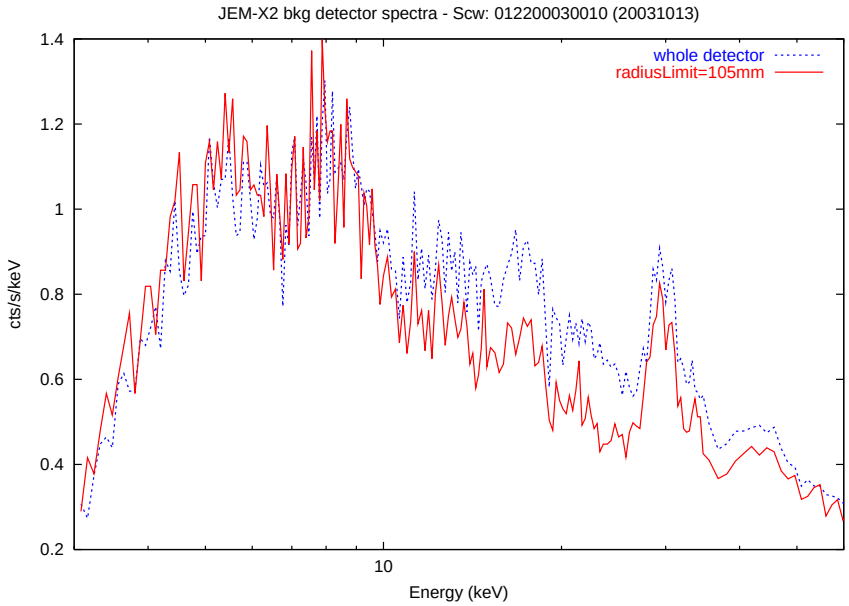

Figure 4.2: JEM–X2 detector spectrum of a blank field observation for a single science window in revolution 122. The Xe line at 30 keV is visible.

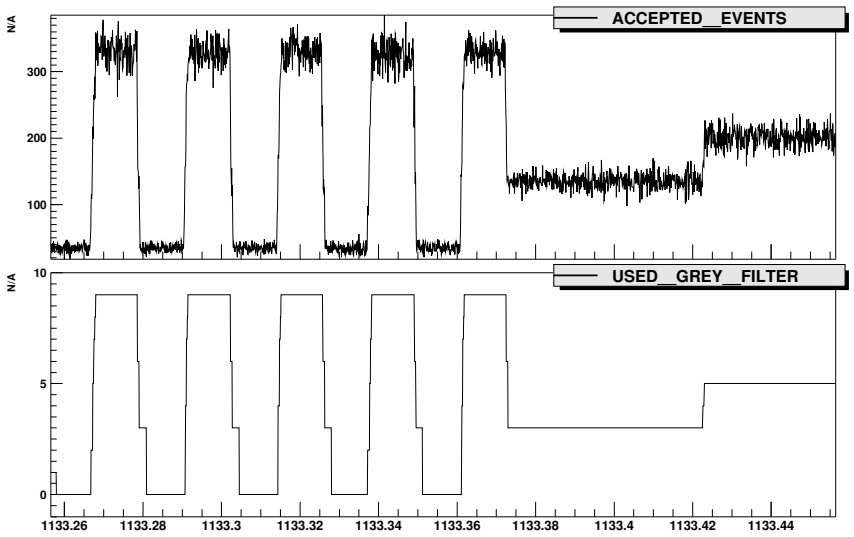

Figure 4.3: Grey filter values and accepted data events for JEM–X

This is the plot seen by ISDC operators in real time – compare with figure 4.4

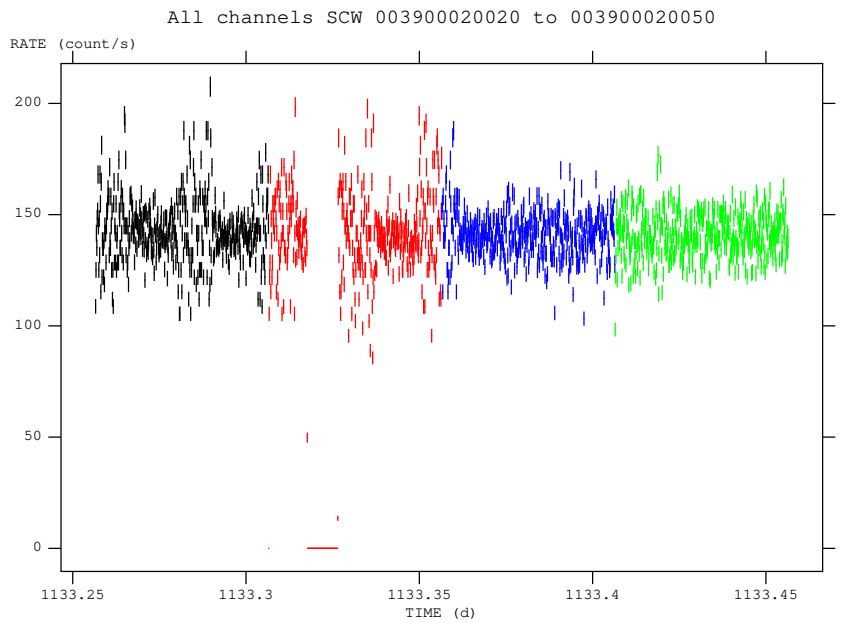

Figure 4.4: Detector lightcurve of Crab observation, revolution 39

Black: ScW003900020020; Red: ScW003900020030; Blue: ScW003900020040; Green: ScW003900020050

Chapter 5

Imaging

The initial coarse image construction produces a sky image covering the entire field of view. X-rays sources typically appear as single pixels on the 200×200 image with higher counts than the surrounding pixels. The source finding procedure searches for peaks where the detection significance (sum of peak divided by the RMS value of the immediate neighborhood, see also section 6.2, page 37) exceeds a user-defined limit (parameter `minDetLev`). These 'found source' positions are recorded in a source list that is then passed to the source extraction processing levels (SPE and LCR) so that spectra and lightcurves can be made for each found source.

Figure 5.1 shows the JEM–X1 image of a relatively weak source Cen X–3 in energy interval 6–10 keV in revolution 203 (SWID 020300120010) The processing was performed using the following command line parameters:

```
jemx_science_analysis
startLevel=COR endLevel=LCR skipLevels="BKG" \
BIN_I_shdType=0 \
nChanBins=4 chanLow="45 83 129 160" chanHigh="82 128 159 196" \
IMA_minDetLev=10
```

Parameters `startLevel` and `endLevel` show that the processing started at the first possible step (data correction and calibration) and finished by making lightcurves of the found source. Background subtraction has been omitted using the skipLevels parameter (see Chapter 3). Since `nChanBins` is set to four, four shadowgrams of type 0 (zero) are produced in the indicate PI ranges. In energy they correspond to 3, 6, 10, 15, and 25 keV. All pixels with a count value of 10 above the average surrounding values are flagged as found sources.

There is a new option with OSA4, namely to get fine resolution images where the angular resolution is 1 arcmin. It requires a shadowgram of type 1 (one) and the selection of the fine resolution option, i.e. `BIN_I_shdType=1 IMA_fineResol=yes`.

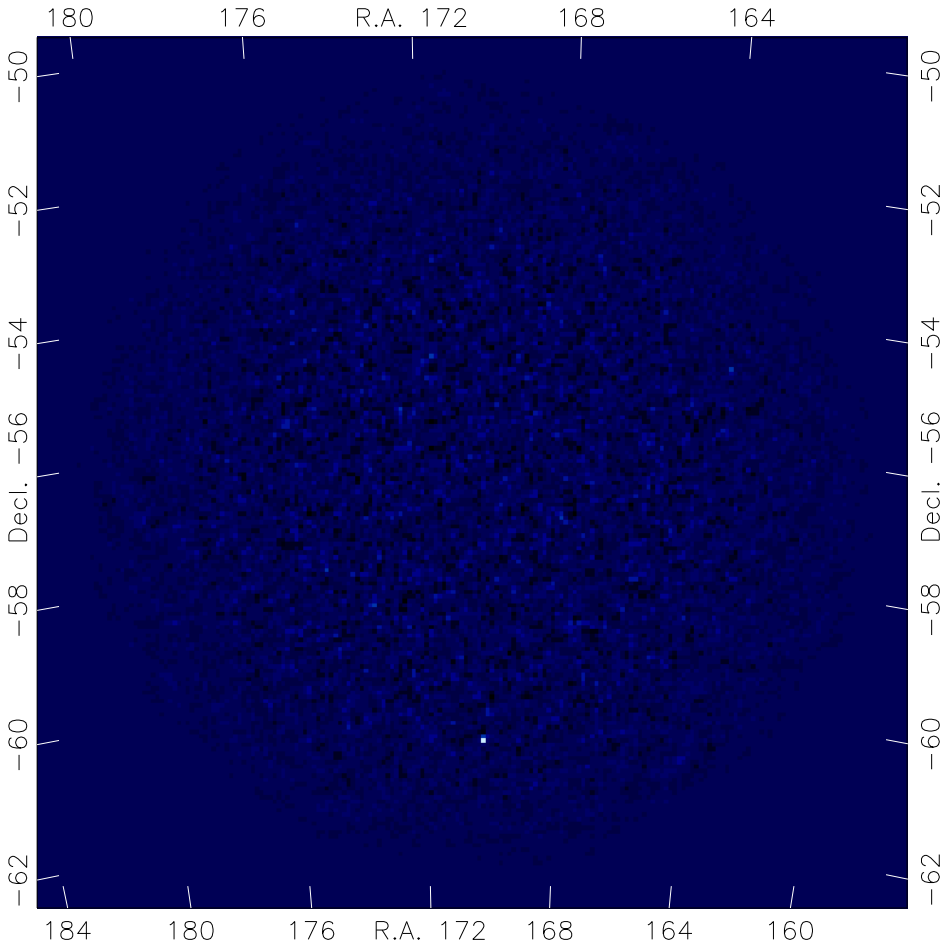

Figure 5.1: Image of Cen X–3 by basic reconstruction (`j_ima_basic_recon`).

The same pointing is shown in Figure 5.2. In none of the cases the vignetting correction has been applied; it causes the noise towards the edge of the image to overwhelm the impression of the image.

The unit of the pixels is counts per second per pixel and the flux is derived by summing the pixels in the peak. Then a correction factor of about 1.5 must be applied to correct for effects such as events not attributed to the source because they accidentally are recorded in a position scattered away from expected.

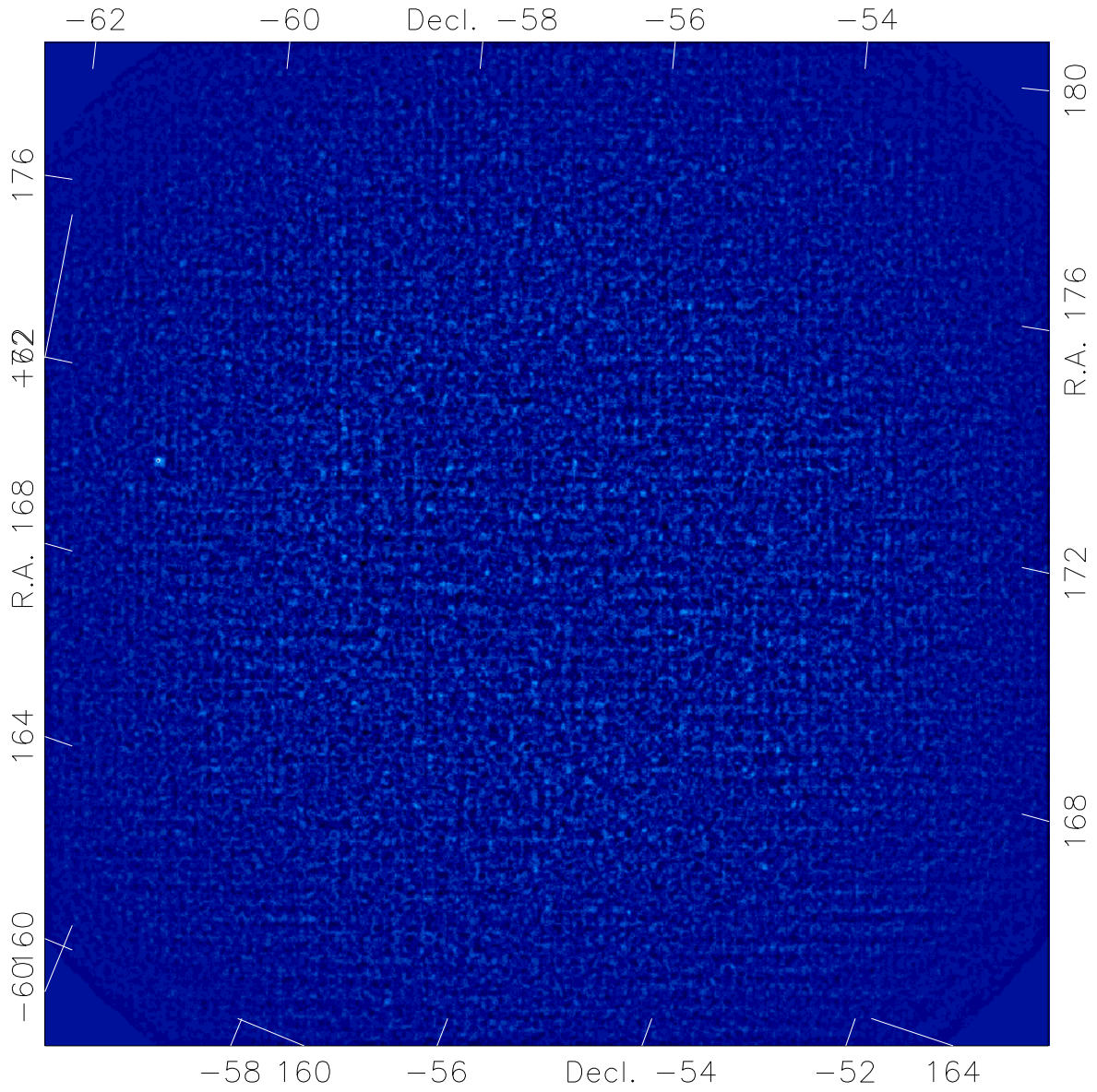

Figure 5.2: Image of Cen X–3 by fine resolution reconstruction (`j_ima_fine_resol`).

Chapter 6

Source detection

The basic task of the scientific analysis is to find X-ray sources from sky images, and then go on to create source spectra and light curves. Consequently source detection is probably the most important aspect of the scientific analysis for general users. The imaging level (IMA) in the scientific analysis does several things when it writes a list of found sources. Each found source is matched with a known catalogue source if possible or flagged as unknown. The found position and the error on the position are also provided in the source list, along with an estimate of the source's flux and detection significance. Each of these issues will be addressed in turn.

6.1 Source positions

Figure 6.1 shows for both JEM-X instruments the scatter of found source positions around the known position of the Crab nebula. The central square shows the catalogue position of the source, and the crosses indicate the position as found by the science analysis software. Error bars on the square show the 1 arc minute minimum uncertainty returned by the analysis software for detected sources. Individual error bars for each source determination are not shown for clarity. The distribution of position errors as a function of angle between source direction and pointing position is shown in figure 6.2.

The two figures demonstrate that for JEM-X1 the misalignment matrix is accurate to less than $10''$for on-axis sources, while for JEM-X2 a systematic offset of 10–20 arcseconds remains. The uncertainties in the position determination grow with increasing off-axis angle. The distributions (fig. 6.2) indicate a systematic component of 10-20 arcseconds, for off-axis sources plus increased scatter which appears to be mainly a function of the decreased significance of the peak – see also figure 6.3.

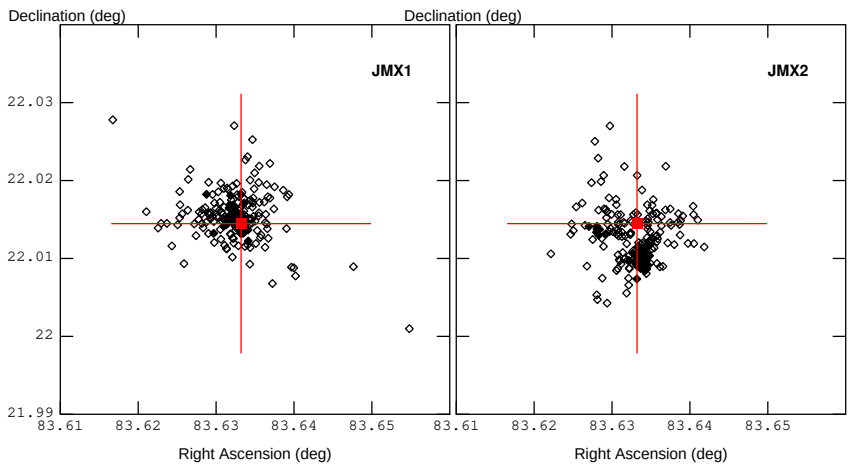

Figure 6.1: Found position deviations of Crab in many pointings. See text for explanation.

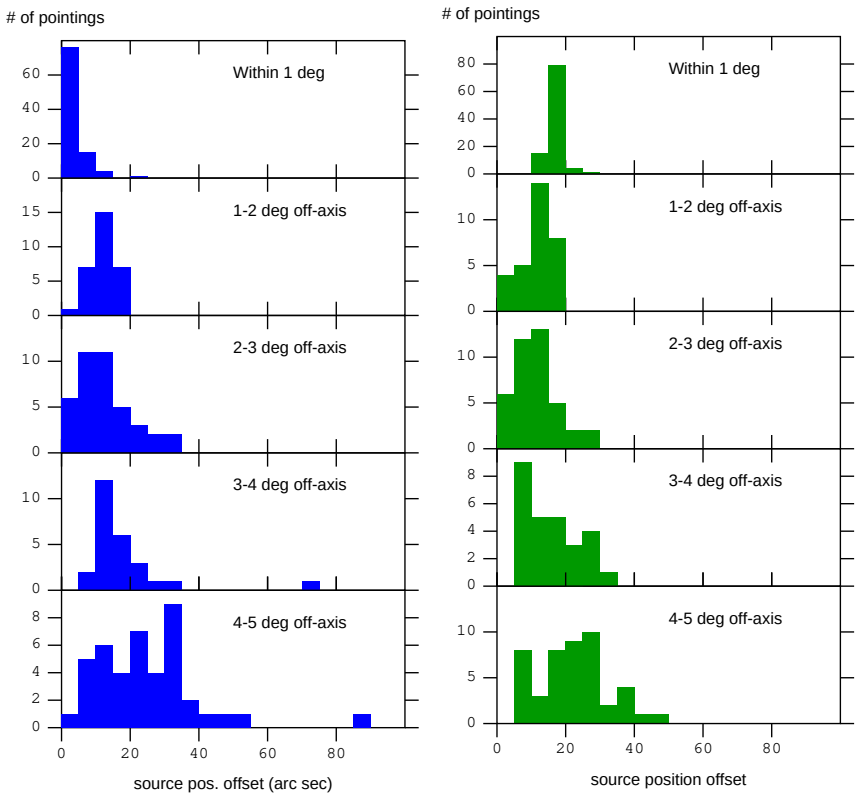

Figure 6.2: Distribution of position deviations of Crab as a function of off-axis angle – left: JEM-X1, right: JEMX-2. See text for explanation.

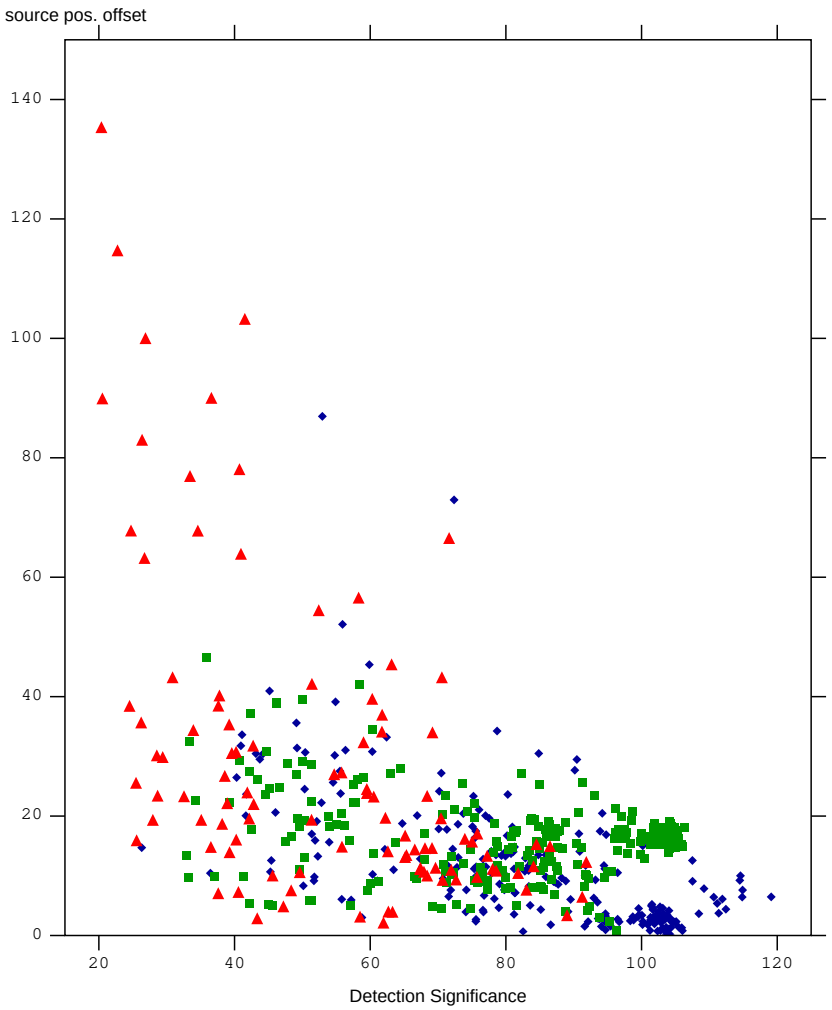

Figure 6.3: Position deviations of Crab and Vela X-1 as function of detection significance – blue diamonds: Crab (JEMX 1), green squares: Crab (JEMX 2), red triangles: Vela X-1 (JEMX 2). See text for explanation.

A similar investigation has been carried out using Vela X–1 as reference. Figure 6.4 shows the results in the same fashion and it is apparent that the position errors are larger due to the smaller number of counts in the peak in the image.

In summary, for sources observed close to the pointing axis, within $\sim$2 degrees, the overall position uncertainty (90% level) is $\sim$20 arcseconds. This rises to $\sim$40 arcseconds between 2 and 4 degrees and $\sim$80 arcseconds for off-axis angles $>$4 degrees.

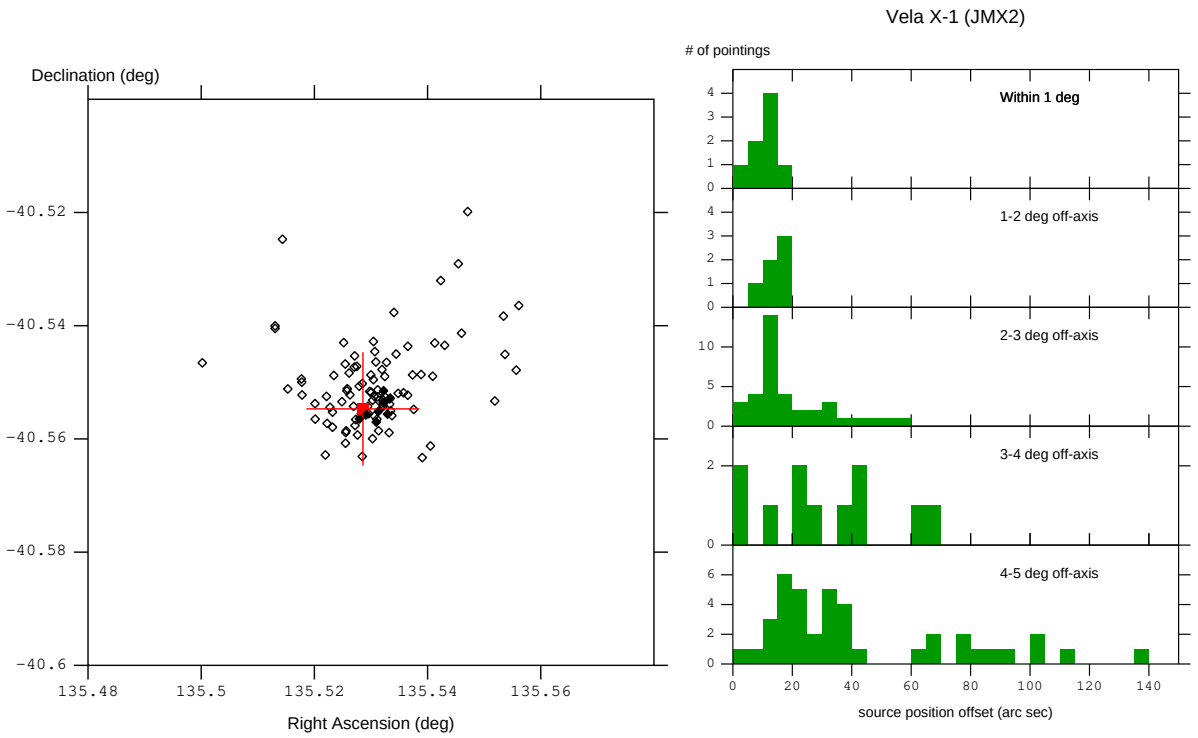

Figure 6.4: Position deviations of Vela X-1 in a part of a 25 point dither. The left panel shows a scatter plot of found positions versus the real position; the right the distribution of position errors as function of off-axis angle. See text for further explanations.

6.2 Source detection significance

The source detection significance is the number of counts in the peak in the image divided by the RMS of the immediate surroundings. The image deconvolution leads to a distribution of pixel values that is not normal. Hence the detection significance cannot be regarded as a “number of sigmas”. Actually the probability getting a source detection significance between 10 and 14 from fluctuations alone is not negligible. A reasonable limit would be around 16. The imperfections of the detector also contribute to the scatter in the image.

Each found source is described in the found source list, JMXi-SRCL-RES, by the detection significance. As expected this value decreases with increasing off-axis angle, however, as figure 6.5 shows for the Crab detections in revolutions 39–44, there is also a large scatter in the significance of different detections at the same angle. This is probably related to the flux determination variations discussed below.

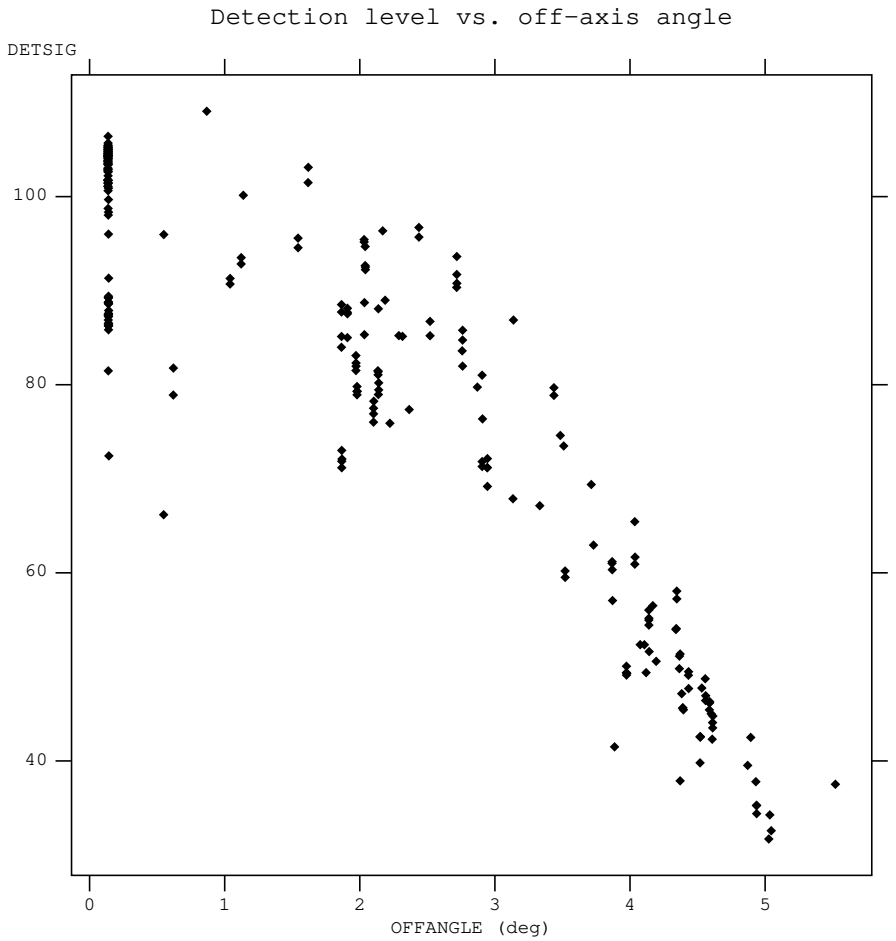

Figure 6.5: Significance of Crab detections with off-axis angle

6.3 Source fluxes

Perhaps the biggest uncertainty in the JEM–X scientific results arises with the source flux estimates. This problem has been traced by the instrument team to the currently quite crude resolution of the vignetting map JMXi-VIGN-MOD, which will clearly have to be improved, and the uncertainty in found source positions. The latter uncertainty will be decreased by improved imaging techniques and the use of background subtraction.

Figure 6.6 shows how the estimated flux of the Crab varies with off-axis angle for revolutions 39–44. Two energy bands are shown 3–10 keV (black) and 10–40 keV (red). The wide scatter on these values still needs to be worked on, and one problem area is clearly the vignetting correction, which may be responsible, among other things, for the suspicious peak at 3°off-axis angle, which is where the slope in the vignetting curve suddenly drops down.

Another correction that is applied to the raw detector fluxes is the deadtime correction. This could conceiveably be a source of error in the absolute flux estimates. Figure 6.7 shows how the on-axis flux determinations for the Crab vary with the deadtime value used for correction. Curiously enough, the scatter of flux values appears to lessen where the deadtime correction is greatest. Note that the deadtime without grey filter losses hovers between 10 and 20% .

Clearly more work is required in this area, both on the raw detector flux determination done during imaging, and on improving the corrections applied to the raw fluxes. Most of these improvements (imaging, background determination, vignetting and event rejection) are expected to be included in the next OSA release (see Chapter 8).

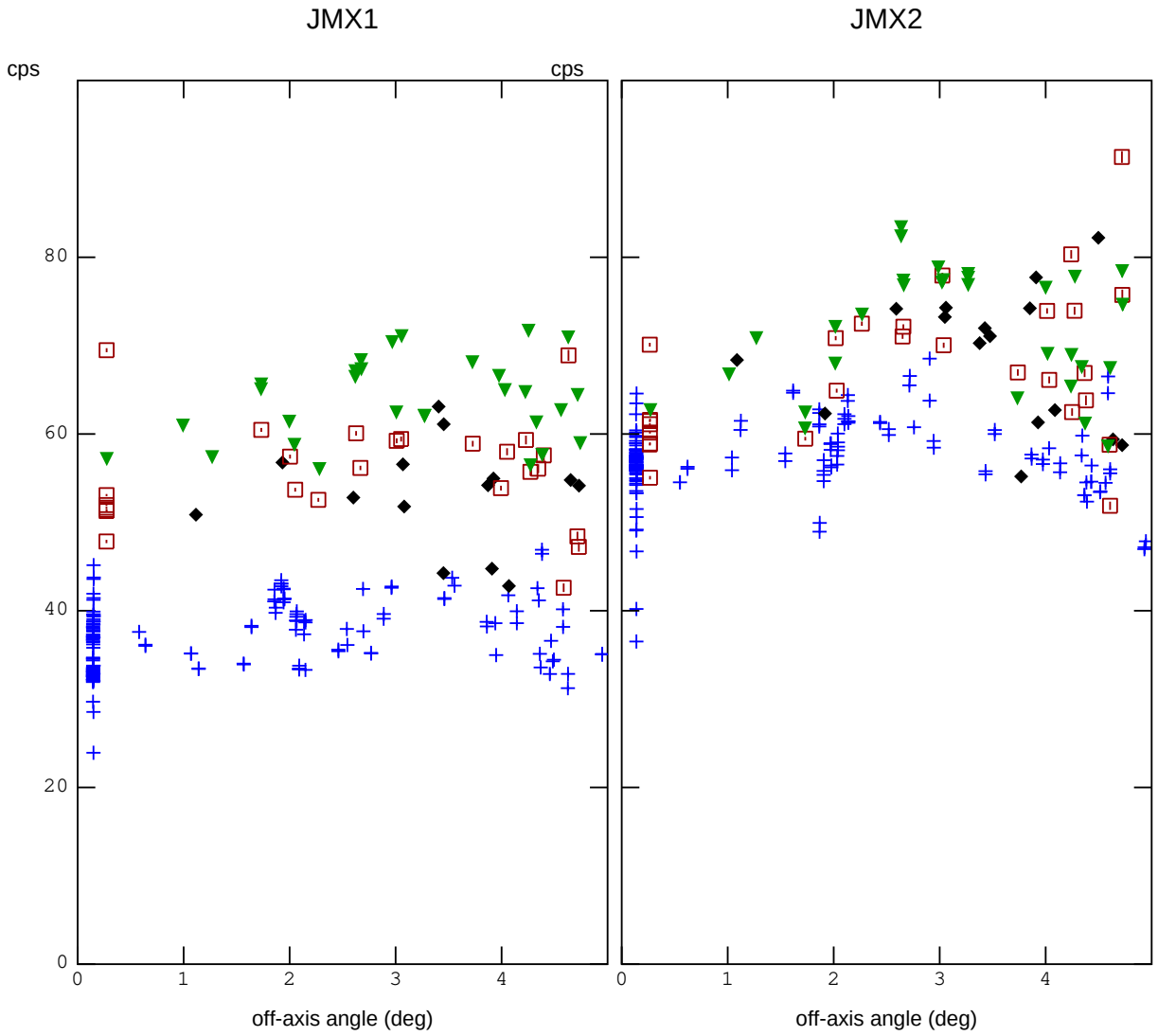

Figure 6.6: Flux of Crab with off-axis angle. The various symbols represent periods of different instrument configurations: blue crosses: rev. 39-44, black diamonds: rev. 45, brown open squares: rev. 102, green inv. triangles: rev 171. The instrument configuration changes that imply changes in these rates are taken into account in spectral responses.

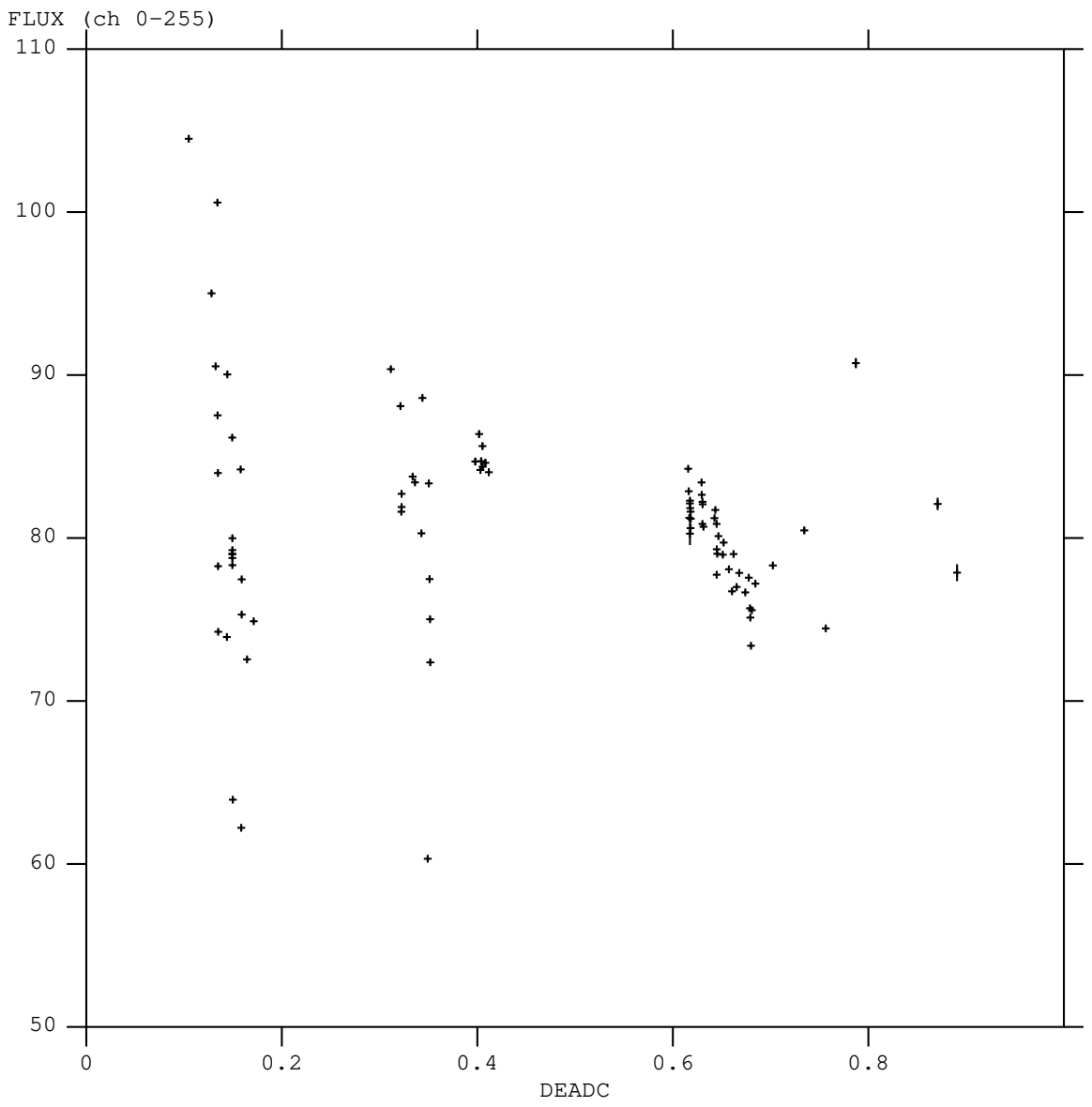

Figure 6.7: Flux of Crab versus instrument deadtime

Chapter 7

Source property extraction

Once sources have been imaged and located, the source extraction steps create spectra and lightcurves of the found sources.

7.1 Source Spectra

The extraction executable `j_src_spectra` uses the information in the source list from the imaging step. With knowledge of source position, instrument geometry (mask, collimator and detector) and the physics of photon interactions the expected illumination on each detector pixel (Pixel Illumination Fraction, PIF) is computed. Since detector resolution depends strongly on energy, PIF-maps are computed at 10 different energies (optionally 18) and then interpolated to intermediate energies. For each energy channel the source flux is extracted by comparing the contrast of the observed shadow pattern with the predicted PIF-map.

The contrast of the PIF-map depends strongly on energy and on off-axis direction. Incorrect modelling of detector resolution can therefore cause distortions of the extracted spectra. For OSA4.0 software these effects are typically seen in sources more than 4 degrees off-axis.

The spectra extracted by `j_src_spectra` are always background-subtracted so in the fitting step e.g. with XSPEC, no background spectrum should be subtracted.

All extracted fluxes have associated error estimates. At present only statistical and not systematic error estimates are given. For single science windows statistical errors dominate in most cases over systematic errors. When many spectra are added however, systematic errors do become important.

7.1.1 The Crab Nebula as calibration source

The Crab Nebula can be observed around February and August and every half year a calibration compaign has been conducted (revolutions 39-45, 102, and 170). A list of periods with constant calibration is given in the JEM–X Analysis User Manual [2], see also p. 3.

Spectral response data have been created based on the original pre-flight response and the observed spectra during the Crab calibration observations. Due to the systematic effects introduced by the spectral extraction methods these responses are currently tied to a given version of `j_src_spectra` ($\geq$4.0 for OSA4).

Figures 7.1 and 7.2 show results of spectral fits to the spectra obtained with individual Science Windows. They demonstrate good stability of the results up to $\sim$4 degrees; at larger off-axis angles results are much less reliable.

At the time of writing, the Crab calibration is considered good in the energy range 5–20 keV. Figure 7.3 demonstrates the remaining strong deviations at low energies which are very much dependent on the exact instrument configuration.

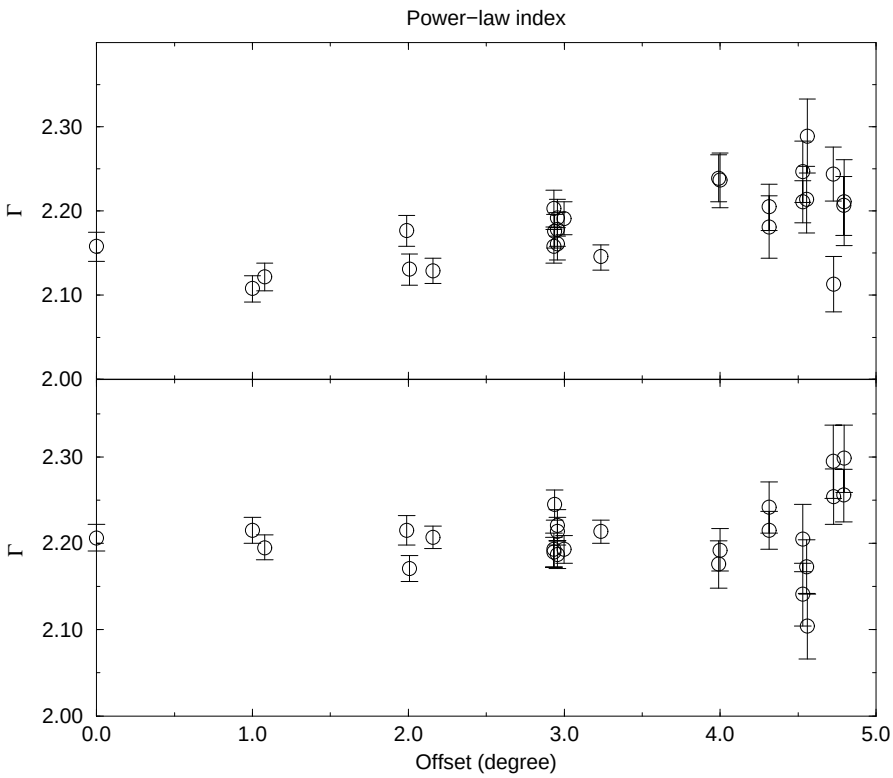

Figure 7.1: Crab spectral slope versus off-axis angle for JEM-X1 (top) and JEM-X2 (bottom).

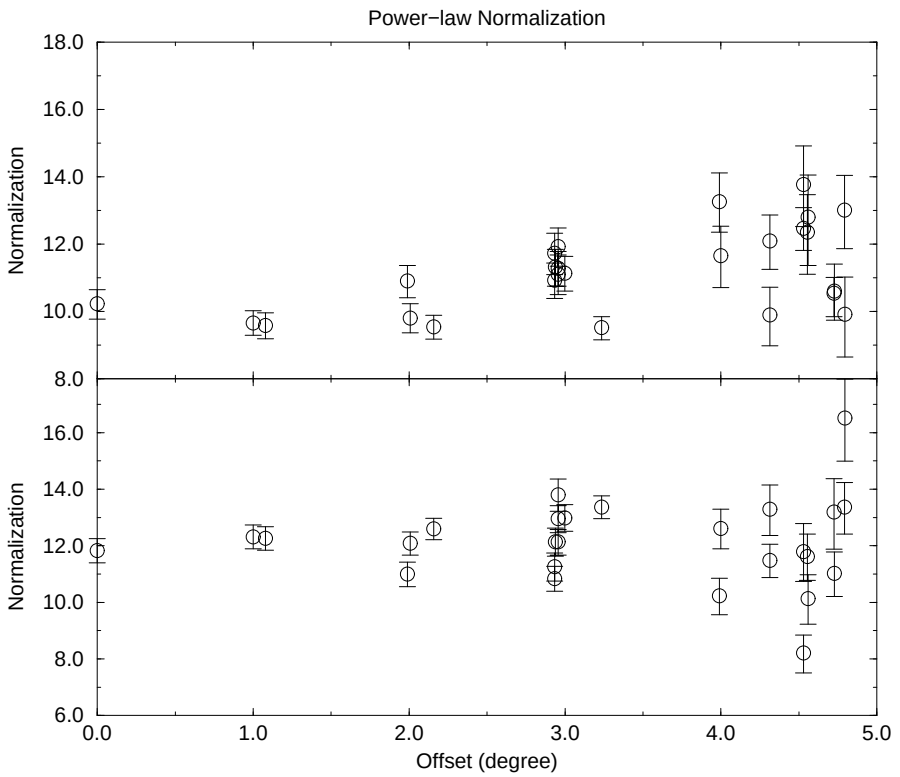

Figure 7.2: Crab normalization versus off-axis angle for JEM-X1 (top) and JEM-X2 (bottom).

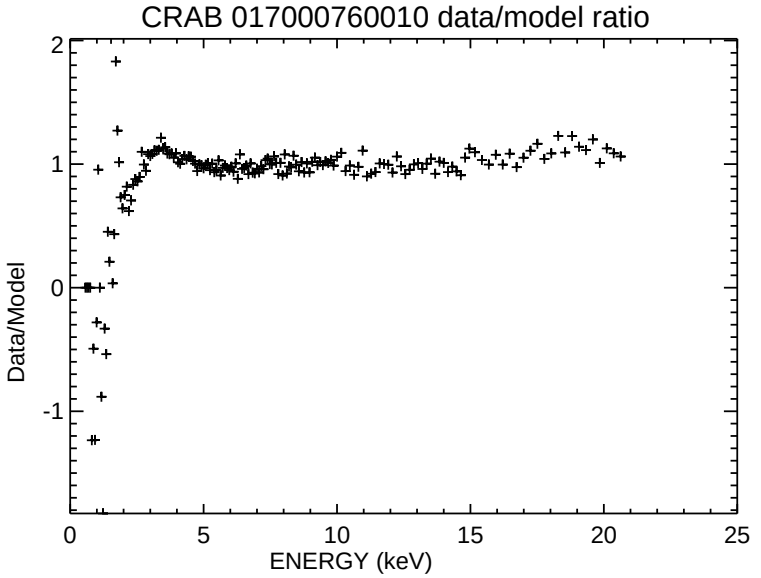

Figure 7.3: Systematic deviations from the expected shape of a Crab spectrum for a single pointing using JEM-X2 data.

7.1.2 The spectrum of a weak source

As an example of source extraction for a weak source we will use source EXO2030+375 which was detected by `j_ima_src_find` with a detection level (significance) of 29.3, and average flux of 2.14 ± 0.05 counts/s.

Using the standard source extraction software the spectrum shown in figure 7.4 was obtained. Each vertical error bar in the figures indicates a 1σ result, so it is clear that even for a fairly weak source we can make a 4–5 σ determination of the continuum. At very low energies the effect of decreased detector sensitivity can also be seen. This arises from two sources, the decreased transmission of the Be window and the event rejection performed by the onboard low level discriminator to control electronic noise in the data.

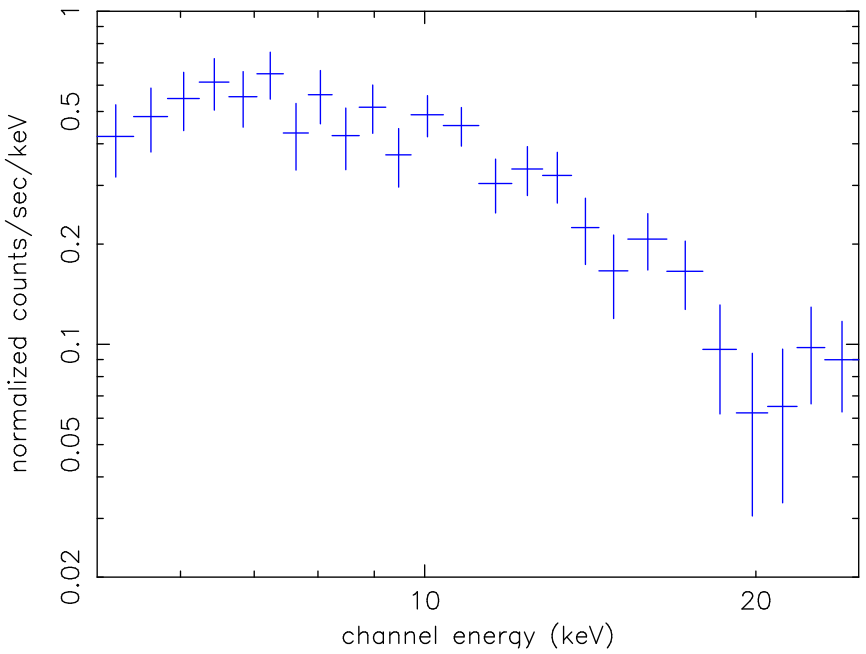

Figure 7.4: Spectrum of EXO2030+375 in the range 5 to 25 keV

7.2 Source Light Curves

Figure 7.5 shows the pulse shape of the faint source EXO2030+375 already discussed. The basis for this analysis was the lightcurve extracted by the ISDC software, which was then processed using the ftools **efsearch** and **efold** to find the best period (41.6 ± 0.1 s) and make the pulse profile. The best results were achieved using a bin length of 1.3 s. All the comments that applied to the spectral analysis should be taken into account for this data also.

Results for a strong source (i.e. suitably complicated by grey filtering) are shown in figure 7.6. This is the form in which the standard data products are produced by the OSA.

For a strong source such as the Crab, typical results of a timing analysis are seen in figure 7.7, which shows the chi-squared of Crab lightcurve data from revolution 39 for various folding periods. The best fit period determined by the folding analysis was then used to create the pulse profile seen in figure 7.8.

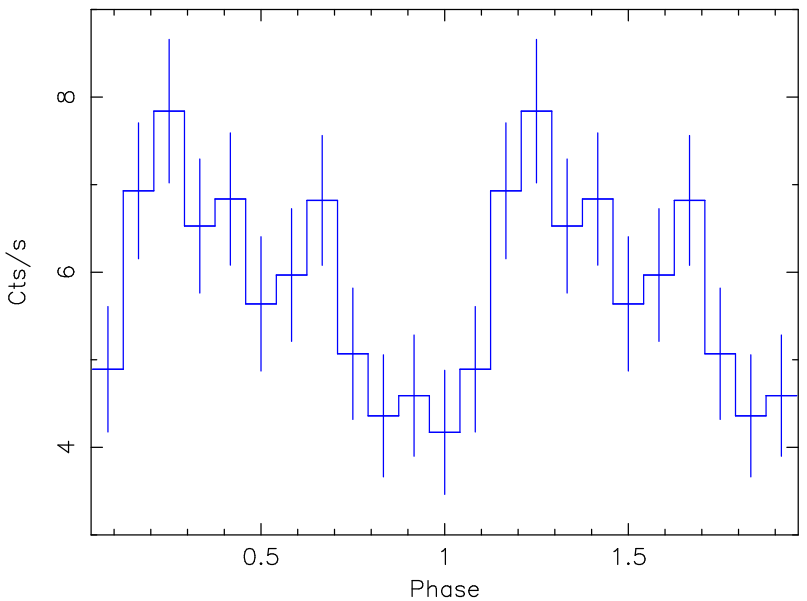

Figure 7.5: Pulse profile of EXO2030+375

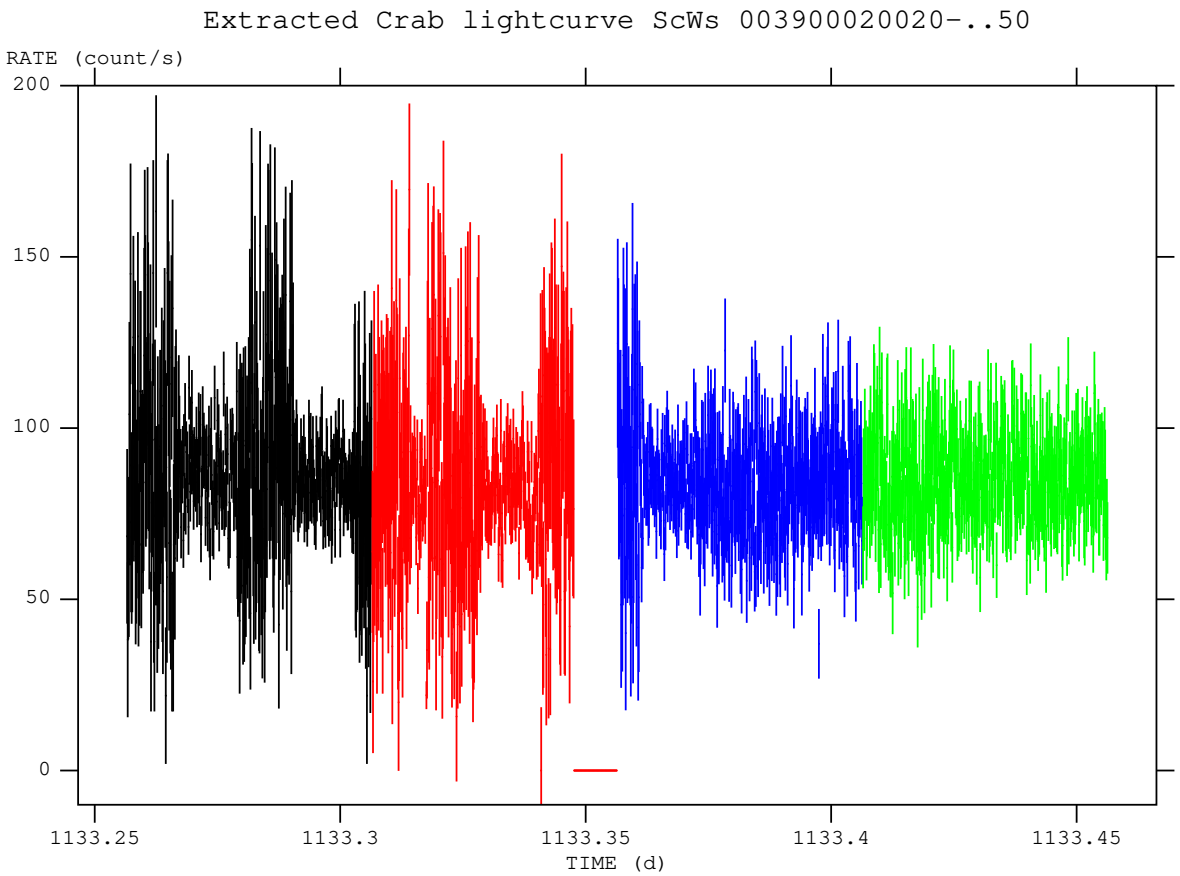

Figure 7.6: Light curve of Crab pulsar in revolution 39

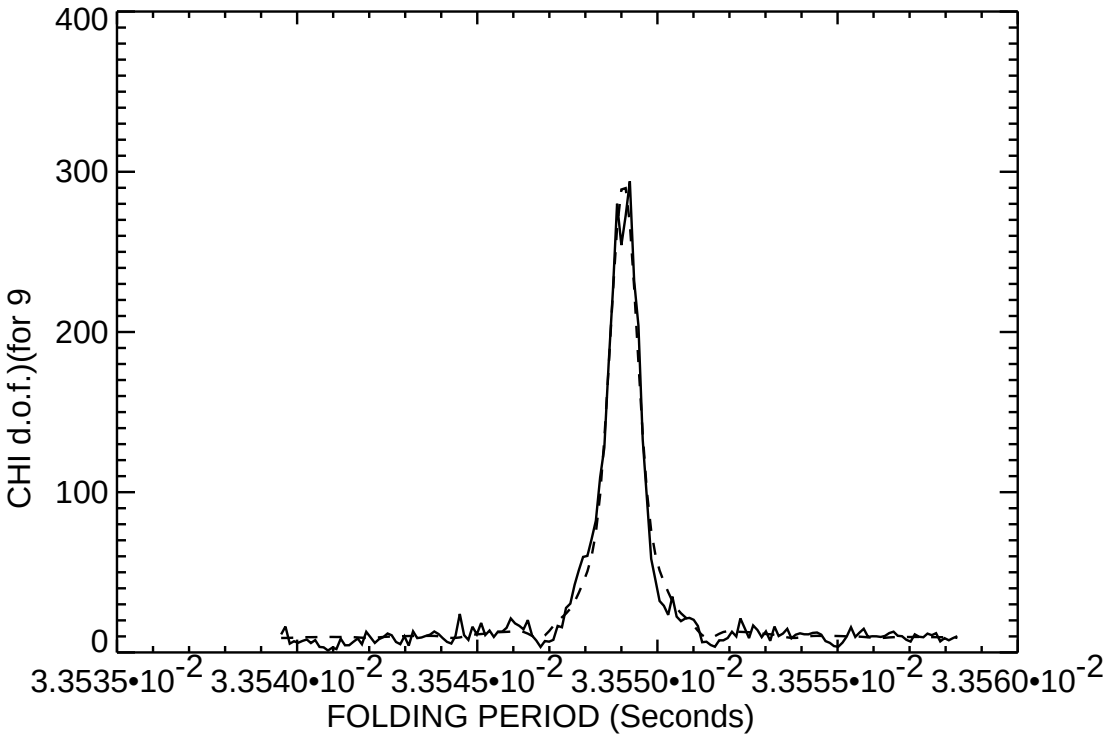

Number of test periods: 160
Number of folding bins: 10
Fold harmonic: 1
JD zero point: -0**********

FOLDING RESULTS:

Probability of peak being noise: *.***e-57
Fitted period: 3.354906e-2 +/- 1.000e-1
Fitted amplitude (relative): 1.129e-1 +/- 1.000e-1
Fundamental period: 3.354906e-2 +/- 1.000e-1

Figure 7.7: Period folding analysis of Crab pulsar in revolution 39

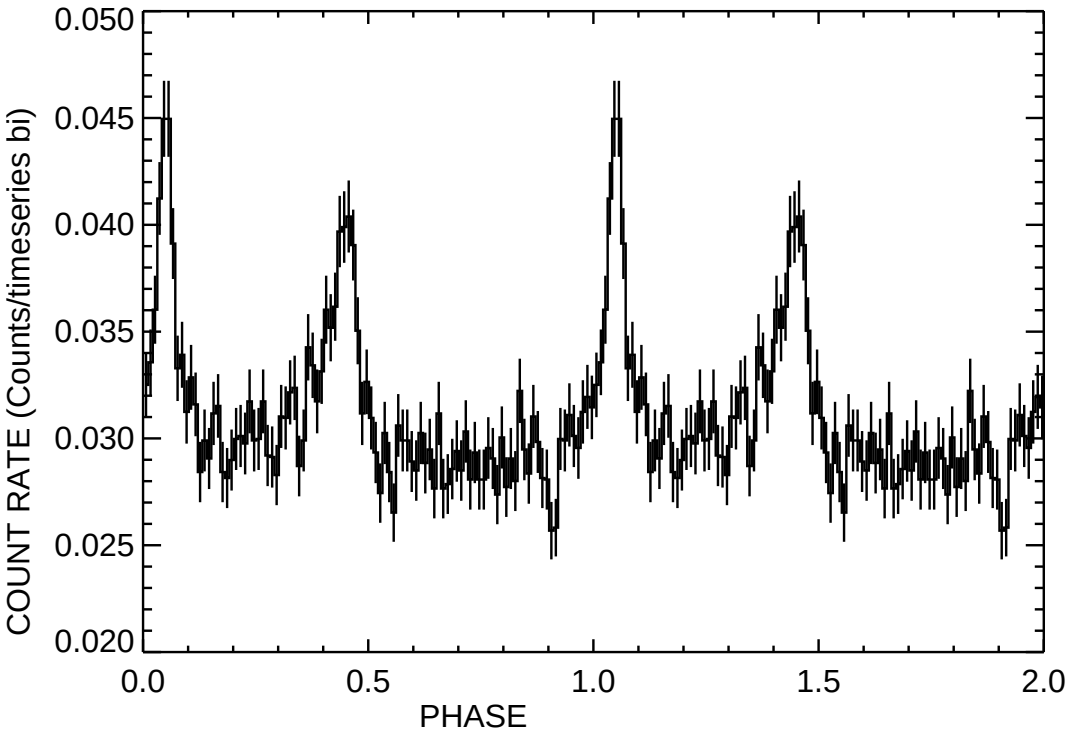

FOURIER COMPONENT	AMPLITUDE (CTS/TIME-BIN)	TIME OF PHASE ZERO
1	1.6754e-3 +/- 2.1e-4	358.95546823 +/- 0.00
2	2.1496e-3 +/- 2.1e-4	358.96768788 +/- 0.00
3	2.2804e-3 +/- 2.1e-4	358.96624838 +/- 0.00
4	3.4900e-4 +/- 2.1e-4	358.96228160 +/- 0.00

Figure 7.8: Pulse profile of Crab pulsar in revolution 39

7.3 Error estimates

Since the source extraction procedure is basically a matter of counting and scaling events, uncertainties in derived rates are estimated by tracing of Poisson errors. An example of a lightcurve for a bright source is shown in Figure 7.9. The error estimates are based on the assumption of many counts per bin, which is valid in this case. This is verified by a chi-square fit of a mean level (solid line). The fit gave a Chi-square of 152.5 for 152 degrees of freedom.

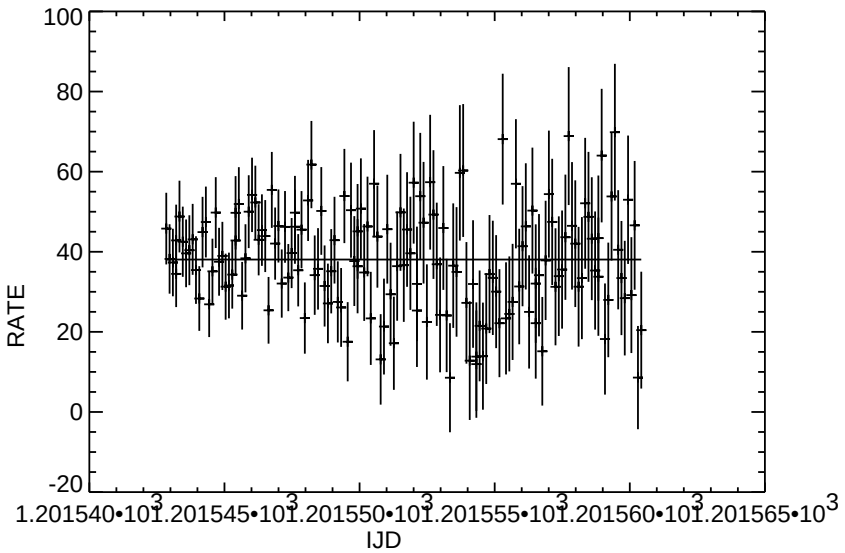

Figure 7.9: Error bars of a bright source

If the number of counts per bin becomes very small the assumptions of the error estimates are no longer valid. Since the open and closed area rates have different relative error the noise fluctuations in the background subtracted source rates will tend to have larger errors when the value is high and smaller when it is low. An example of this is shown in Figure 7.10. Because of this systematic difference in error bars a Chi-square fitted curve will be draged toward the lower values. In this case the assumption that all data bins have the same error will be more correct. See Chi-square fit in Figure 7.11 where the errors have been changed to a constant using ftool commands. The problem can be avoided by using longer lightcurve bins.

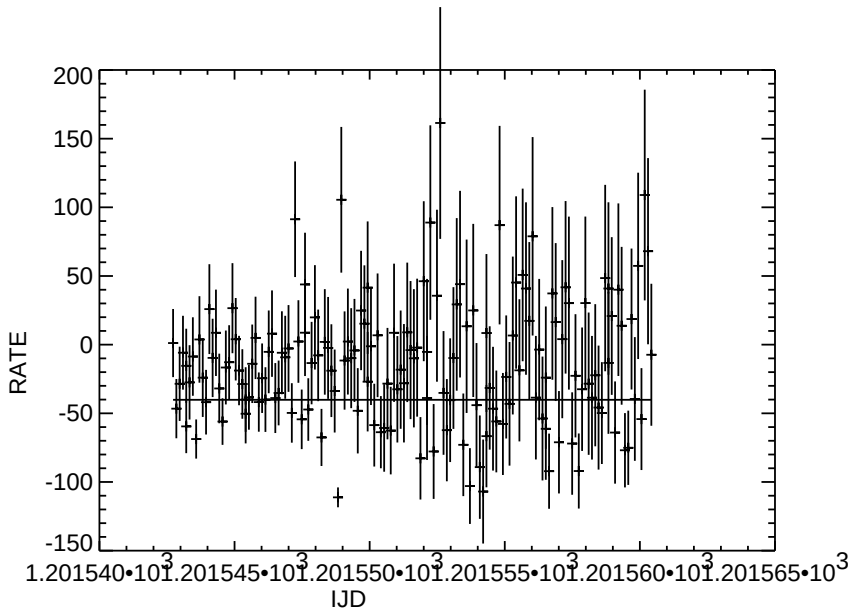

Figure 7.10: Error bars of a faint source, errors assigned as in the case of a strong source

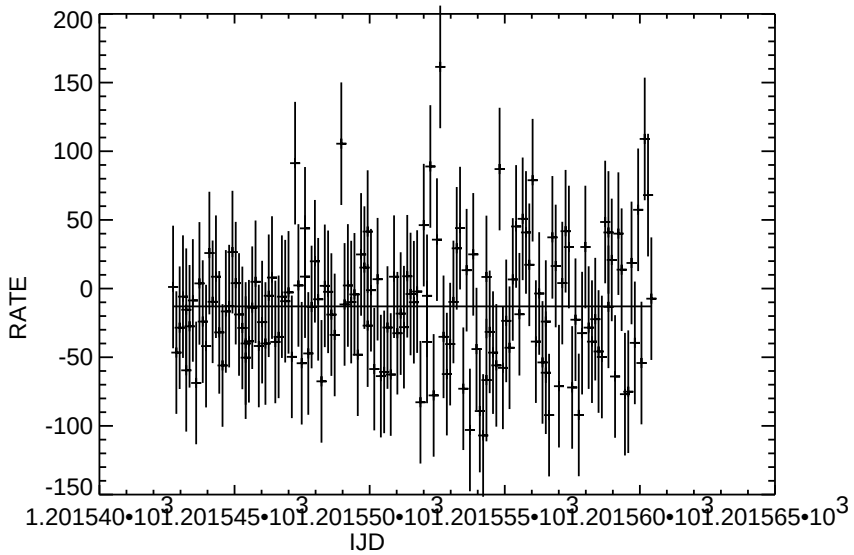

Figure 7.11: Error bars of a faint source, all databins have identical errors

Chapter 8

Future Improvements

The results presented here clearly show that the current release of the JEM–X Science Analysis Software which is part of ISDC OSA, is capable of delivering the science data products that were planned before launch. Future updates will happen but their implementation will not affect the way the software is to be used by the community, only the nuts and bolts of the algorithms and methods used by the various programs.

If any particular areas require major improvement, it would be in source detection and flux estimates, which will require refining and improving many different aspects of the science analysis software. Also some changes are being forced on the system by unexpected detector behaviour (e.g. weak Ni lines in the calibration spectra, dead anodes, increase of gain, and detector resolution degradation).

Some of the changes listed here are quite technical and need not worry the general user, but all can be expected to improve the quality of the JEM–X science data products:

Refined imaging New imaging software is being developed, including a mechanism for iterative removal of sources to improve the sensitivity of the instrument for automatic source detection. This will enable weaker sources to be detected with more accurate position determinations, even in the partially coded field of view.

Background handling Determination of the amount of diffuse and instrument background is based on a catalogue of models of background spectra mapped onto the different areas of the detector. Until a good catalogue of background models has been created the background handling step of the processing cannot be performed in a way that improves the scientific results. Now that the majority of the software changes and configuration changes are complete the catalogue is being created from empty field observations. Background subtraction before image deconvolution will increase instrument sensitivity for weak sources and improve flux estimates, source spectra and lightcurves.

Vignetting Considerable variations in flux determinations are seen in the source detection results, and these have been traced back to the currently low resolution of the vignetting table, and uncertainty in source positions, both of which affect flux values very strongly. It is clear that the vignetting table is going to have to be redelivered with better resolution. Improved imaging techinques should help to decrease source position uncertainties.

Source positions The systematic 15-20$''$ source position offset needs to be tracked down (possibly in the ISDC misalignment matrix) and dealt with.

Detector binning Problems with light curve countrates for time bins immediately next to data gaps and science window boundaries have to be investigated and corrected.